

Multi-dimensional Features of Neutrino Transfer in Core-Collapse Supernovae

K. Sumiyoshi

Numazu College of Technology, Ooka 3600, Numazu, Shizuoka 410-8501, Japan

`sumi@numazu-ct.ac.jp`

T. Takiwaki

National Astronomical Observatory of Japan, 2-21-1 Osawa, Mitaka, Tokyo 181-8588,
Japan

`takiwaki.tomoya@nao.ac.jp`

H. Matsufuru

Computing Research Center, High Energy Accelerator Research Organization 1-1 Oho,
Tsukuba, Ibaraki 305-0801, Japan

`hideo.matsufuru@kek.jp`

and

S. Yamada

Science and Engineering & Advanced Research Institute for Science and Engineering,
Waseda University, Okubo, 3-4-1, Shinjuku, Tokyo 169-8555, Japan

`shoichi@heap.phys.waseda.ac.jp`

Received _____; accepted _____

Submitted to Astrophysical Journal Supplement

ABSTRACT

We study the properties of neutrino transfer inside supernova cores in three space dimensions (3D) by solving the Boltzmann equations for neutrino distributions in genuinely six dimensional phase space (6D). Utilizing the Boltzmann solver with multi-angle, multi-energy group for three species, we investigate stationary neutrino distributions and associated collision terms for representative 3D snapshots at post-bounce stage from the simulations of core-collapse of massive stars. We reveal the genuine characteristic of 3D neutrino transfer such as non-radial fluxes and non-diagonal angle moments with the advantage of multi-angle treatment by an S_n method, which directly describes the angular distributions. In addition, we evaluate the corresponding quantities by the ray-by-ray approximation in the same framework in order to assess deviations from the 6D Boltzmann evaluation. We found that neutrino distributions by the ray-by-ray approach tends to maintain local variations due to environment around the neutrino sphere, leading to persistent influence along the radial ray. The deviations of the densities and fluxes of neutrinos appear at $\sim 20\%$ levels along the ray due to the ray-by-ray characteristics. Deviations of the heating rate between the two methods are less drastic than those in the densities and fluxes, but become significant in some regions. The examination of the ray-by-ray approximation suggests that careful assessment of the influence on 3D supernova dynamics is necessary with different levels of approximations and methods. Detailed information on the angle and energy moments in our framework is profitable for future development of numerical methods in neutrino-radiation hydrodynamics.

Subject headings: methods: numerical — neutrinos — radiative transfer — stars: massive — stars: neutron — supernovae: general

1. Introduction

Neutrinos perform an essential role in the mechanism of core-collapse supernovae as a driving force for dynamics starting from the gravitational collapse of massive stars. Transport of energy and composition via the neutrinos is crucial to determine their fate; supernova explosions with an energy of 10^{51} erg (Bethe 1990; Kotake et al. 2006; Janka et al. 2007). In the collapse, the neutrinos are produced from electron captures and trapped inside the central core as pressure support. Pairs of neutrinos are created as the thermal energy converted from the gravitational energy. The emission of the trapped neutrinos results in an energy release of $\sim 10^{53}$ erg in the form of supernova neutrinos. The release of huge energy in neutrinos is vindicated by the observed events from SN 1987A (Hirata et al. 1987). The properties of emitted neutrinos carry valuable information of the mechanism of explosion, dense matter inside compact stars and progenitors (see Nakazato et al. (2013), for example, and references therein).

The interaction of the neutrinos with material in the supernova core contributes to the energy transfer in a significant size. A portion of the emitted neutrinos is absorbed by the matter behind the shock wave. This leads to the heating of material to assist the revival of the forward propagation of shock wave. The shock wave stalls after the initial launch under spherical geometry and hovers above the proto-neutron star due to the hydrodynamical instabilities in multi-dimensions. The so-called neutrino heating mechanism (Bethe & Wilson 1985) is one of plausible ways to trigger the explosion on top of the asymmetric evolution of shock wave under a marginal condition. In fact, energy gain by the neutrino heating amounts to $\sim 10^{51}$ erg, which is comparable to the explosion energy of observed supernovae (Janka & Müller 1996). How the neutrino heating mechanism acts as an essential cause of explosion with other important effects remains an unsolved issue. Detailed studies of hydrodynamical instabilities with the neutrino heating as well as the

other scenarios (ex. acoustic mechanism, magnetically-driven mechanism) are necessary to settle a long standing issue of the explosion mechanism for decades (Janka et al. 2012; Burrows 2013).

In order to pin down the cause of multi-dimensional explosion under the influence of neutrinos, the careful evaluation of neutrino heating and cooling is necessary. At center, the neutrinos interact frequently enough and diffuse out gradually inside the proto-neutron star just born after the bounce. The emission of neutrinos acts as cooling of matter at surface layers accreting on this nascent object. The partial absorption of the emitted neutrinos takes place between the neutrino sphere and the stalled shock wave before they stream out freely. Transfer of energy from neutrinos to matter contributes to the heating through the absorption processes. Detailed information of the neutrino-matter interaction in this region with convective motions is important to understand the cooling and heating processes.

The evaluation of neutrino transfer is mandatory to provide the rate of cooling and heating since they proceeds in the intermediate situation between the diffusion and free-streaming regimes. As for cooling, the flux and energy spectra of escaping neutrinos are determined by the neutrino-matter interactions around the energy-dependent neutrino sphere. It is necessary to solve the neutrino transfer for multi-energy groups since the interactions strongly depend on the neutrino energy. In order to evaluate the heating rate, the flux of neutrinos, the energy and angle spectra as well as the neutrino reactions in the heating region are influential quantities. The angular distribution of neutrinos is especially an important factor to determine the heating rates besides the flux and energy spectrum mainly determined in the cooling region. While the neutrinos are isotropic at center and forward-peaked outside, the angular distribution in the heating region is non-trivial in a transitional situation.

The exact treatment of neutrino transfer is, therefore, highly advisable to describe the

energy and angle distributions. However, the approximate methods of neutrino transfer have been adopted in most of numerical simulations of supernovae in multi-dimensions. This is because the full description of neutrino distributions requires six-dimensional phase space (three spatial coordinates and three momenta of neutrinos), which is formidable even for modern supercomputing resources. While computations in multi-energy group are standards nowadays, approximations of angular distributions have been usually made in multi-dimensional simulations. Since the exact treatment of neutrino-radiation hydrodynamics under spherical symmetry has become possible, the influence due to the approximations of neutrino transfer has been extensively studied through comparisons between the exact and approximate methods (Janka 1992; Messer et al. 1998; Yamada et al. 1999; Liebendörfer et al. 2005). It is well known that the diffusion approximation with a flux-limiter overestimates the degree of forward-peak and thus underestimates the heating rate. Although the difference is not drastic, a slight modification of heating may be crucial for triggering the explosion under the marginal conditions (Janka & Müller 1996).

Evaluation of approximate methods of the neutrino transfer in multi-dimensions has growing importance under the current circumstance of supernova studies with competing effects, including possible modifications of heating rate in multi-dimensions. The diffusion approximations (including its variants such as IDSA) and ray-by-ray methods are used in the state-of-the-art 2D/3D simulations. While they brought a handful of successful explosions, their approximate treatments of neutrino transfer introduce a certain level of uncertainty. Those approximations should be examined carefully to judge the reliability (or errors) in explosion dynamics as have been established in the various comparisons of spherical simulations.

In principle, there is movement to shift the method from approximate to exact ones in multi-dimensions, having rapid advance of supercomputing resources. In two dimensions,

multi-angle and multi-energy-group neutrino radiation-hydrodynamics have been performed to follow the post-bounce evolution of supernova cores (Livne et al. 2004; Ott et al. 2008; Brandt et al. 2011). They adopted a discrete-ordinate (S_n) method to fully describe angle distributions in 2D space (Livne et al. 2004). Ott et al. (2008) demonstrated the ability of the S_n method in intermediate regimes with anisotropy and reported the comparisons with the diffusion approximation. They found the 2D multi-angle transport is superior in describing the neutrino distributions with global asymmetries under aspherical supernova cores. The neutrino flux asymmetries in the polar direction result in the enhancement of local neutrino heating rates along the pole with respect to the those around the equator. Brandt et al. (2011) analyzed further the neutrino radiations in the heating region to find the importance of multi-angle transport. The integration of neutrino transport from many angles leads to less variations of neutrino quantities by averaging out the 2D fluctuations of matter quantities. Such detailed study of the neutrino transfer has been limited in the 2D case of supernova cores under axial symmetry.

Our purpose of the study is, therefore, to explore the basic feature of neutrino transfer in realistic 3D supernova cores, for the first time. Adopting a set of profiles from the 3D numerical simulations (Takiwaki et al. 2012), we examine the neutrino distributions, their transport and energy transfer rates by solving the multi-energy and multi-angle neutrino transfer under the fixed background of matter quantities. The newly developed code of the 6D Boltzmann solver (Sumiyoshi & Yamada 2012) enables us to study the detailed information of energy and angle distributions in important regions for explosion dynamics. We reveal the non-radial (polar and azimuthal) transport in the aspherical and fluctuating matter distributions by the advantage of multi-angle transport in 3D space. This attempt is new in contrast to a sample case (Sumiyoshi & Yamada 2012) adopting the artificially deformed 3D configuration. We examine behavior of the angle moments of the neutrino distributions, which are beneficial to examine the transitional regime beyond diffusion

approximations. Those quantities are also useful for development of numerical codes using the moment formalism.

The 6D Boltzmann evaluation enables us to study the reliability of the approximate methods. We examine the quality of approximate results by the ray-by-ray approach, which is routinely used in many simulations in 2D and 3D, through comparison with the full solution by the 6D Boltzmann solver. By dropping the polar and azimuthal advection, we can simulate the ray-by-ray approach in our code with the same settings for neutrino reactions and profiles. We examine the amplitude of non-radial transport, which cannot be fully described in the ray-by-ray approach, and the importance of the exact treatment in the realistic 3D profiles. As we will show, the contribution of polar and azimuthal fluxes are significant even beyond the region of diffusion regime. We compare the neutrino distributions and heating rate in both the exact and ray-by-ray cases in order to explore whether sizable differences arise in the stage for explosion dynamics. The directional dependence of neutrino distributions in the ray-by-ray approach turns out significant, depending on the profiles, and may affect local rates of the neutrino heating for explosions.

We describe the method to study the neutrino transfer by solving the 6D Boltzmann equation as well as a ray-by-ray approximation in §2.1. We fix the background of matter variables to obtain the stationary distributions of neutrinos for a set of the 3D supernova cores. The 3D profiles taken from the detailed simulations by Takiwaki et al. (2012) are presented in §2.2. We report in §3.1 the basic feature of neutrino transfer in 3D space by showing profiles of density, radial and non-radial fluxes obtained by the 6D Boltzmann solver. The corresponding results by the ray-by-ray approach in our computation are presented in §3.2 to examine the comparisons between the two approaches and the size of deviations due to the approximation. We investigate the profiles of the heating rate by 6D Boltzmann solver and the ray-by-ray approximation in §4.1. We reveal the size of difference

in the heating rates between the two approaches with analysis of variations for the given profile. In §4.2, we present the heating rates for other profiles to demonstrate the general feature of difference between the two methods. We examine the volume integrated heating rate in §4.3 to discuss the global influence in the supernova dynamics. In §5, we show the angle and energy moments of the neutrino distributions obtained by the 6D Boltzmann solver. We discuss results from the ray-by-ray approach and their deviations. Discussions and implication from our study is given in §6 followed by the summary in §7.

2. Numerical settings

2.1. Neutrino transfer in 3D space

We study the neutrino transfer in 3D supernova cores by adopting the numerical code to solve the Boltzmann equation in 6D (Sumiyoshi & Yamada 2012). The code solves the time evolution of the neutrino distributions via neutrino transport and reactions in 3D space and 3D momentum space. We adopt the spherical coordinate system and use neutrino energy and two angles to designate the neutrino momentum. The 6D Boltzmann equation in the conservative form is discretized in a finite-differenced method on the spatial grids as well as multi-energy, multi-angle grids. We take the discrete-ordinate (S_n) method to describe the angular distributions. The implicit differencing is adopted for the advance of time step. This ensures the stability to reach the equilibrium solution after sufficient steps of time evolution for the current purpose. Further details of the numerical scheme as well as a set of 3D numerical tests can be found in Sumiyoshi & Yamada (2012).

A basic set of the neutrino reactions is implemented in the collision term (Bruenn 1985; Sumiyoshi et al. 2005). The set includes the emission, absorption and scattering of neutrinos via nucleon and nuclei. The pair processes via electron-positron annihilation,

creation and the nucleon-nucleon bremsstrahlung are also taken into account. We treat the three neutrino species, ν_e , $\bar{\nu}_e$ and ν_μ , which is a representative of the group for four species ν_μ , $\bar{\nu}_\mu$, ν_τ and $\bar{\nu}_\tau$. The current set of neutrino reactions is essential for the description of the role of neutrino reactions in the supernova mechanism, but a minimum due to the limited computational resources. The electron-neutrino scattering has been omitted in the current study since its effect on the post-bounce phase is minor (Thompson et al. 2003; Burrows et al. 2006). The same set has been used for detailed tests of the 3D neutrino transfer (Sumiyoshi & Yamada 2012) through comparisons with the 1D results of core-collapse supernovae from Sumiyoshi et al. (2005). The modern version of neutrino reaction rates will be implemented in future having enough computing resources. The equation of state of Lattimer & Swesty (1991) are used for the whole calculations in the current study to match with the profiles we adopt from the supernova simulations by Takiwaki et al. (2012).

We investigate the static properties of neutrino transfer by solving the 6D Boltzmann equation for a set of snapshots taken from the supernova simulations. In order to obtain the stationary state, we follow the time evolution of the neutrino distributions by the 6D Boltzmann solver for the fixed background profile. We perform numerical simulations of time evolution for a sufficiently long period (typically ~ 20 msec) until we get the steady state from an initial distribution of sparse neutrinos. Although we adopt snapshots from the dynamical situations, we do not take the effects due to fluid motion. We drop the velocity-dependent terms in the collision term in the current study and neglect the Lorentz effects. Our aim here is to reveal the 3D feature of the neutrino transfer within the zeroth-order of v/c as a first step toward the full treatment. The Lorentz effects such as Doppler shifts of energy and angle aberrations should be carefully studied in future. The implementation of the velocity-dependent terms into the current framework of the Boltzmann solver for the neutrino-radiation hydrodynamics will be reported elsewhere

(Nagakura et al. 2014).

In addition to the calculations by the full solution of 6D Boltzmann equation, we perform approximate calculations by a ray-by-ray prescription in our framework. By dropping off the advection terms due to spatial θ - and ϕ -derivatives as well as neutrino-angle ϕ_ν -derivative in the Boltzmann equation, we can perform computations of the neutrino transfer along independent radial rays in our framework. We examine the size of errors due to the approximation and explore its possible influence on explosion dynamics.

The numbers of mesh points employed for neutrino distributions are $N_r = 256$, $N_\theta = 64$, $N_\phi = 32$ for the spatial grid in our baseline 3D models. The neutrino angle and energy grids are set with $N_{\theta_\nu} = 6$, $N_{\phi_\nu} = 12$ and $N_\varepsilon = 14$. The energy grid is placed logarithmically from 0.9 MeV to 300 MeV with a fine grid for high-energy tails. Computations with this setting of the mesh points are the largest scale, using 1.6TB memory, on 8 node of HITACHI SR16000 at KEK. In order to obtain one configuration of the model after the evolution in several tens of milli-seconds, we typically need a run of $\sim 4 \times 10^4$ steps using the MPI-parallel code of the 6D Boltzmann solver. It takes ~ 200 hours of wall-clock time on 8 node of SR16000 by 128 MPI processes.

The convergence test in Sumiyoshi & Yamada (2012) shows that the current setting of the angle and energy grids are sufficient to obtain the reasonable results. We have checked further the dependence on resolution by increasing the number of grids in some sample models. For this purpose, we perform the numerical simulations for the inner part of the supernova core (≤ 360 km) using $N_r = 128$ to increase one of the angle grids. When we increase the number of the grids for θ_ν from $N_{\theta_\nu} = 6$ to 8, we find typical deviations within 2 % in the neutrino densities, fluxes and heating rate. In the case of increasing N_{ϕ_ν} from 12 to 16, the deviations are within ~ 0.8 %. Appearance of large deviations of the heating rate is limited in the region along the gain radius due to very small values close to zero.

2.2. 3D supernova cores

We utilize matter profiles from the 3D numerical simulations of core-collapse supernovae by Takiwaki et al. (2012). We take snapshots from the post-bounce stage in the evolution from an $11.2M_{\odot}$ star of Woosley et al. (2002). Their numerical simulations were performed by the neutrino-radiation hydrodynamics using the extended ZEUS-MP code for hydrodynamics (Hayes et al. 2006; Iwakami et al. 2008) and the IDSA scheme (Liebendörfer et al. 2009) for neutrino transport with the ray-by-ray approximation.

We adopt the 3D profile of density, temperature and electron fraction from the snapshot and remap onto our numerical mesh. We use the same radial (logarithmically spaced) grids up to 2600 km, taking inner 256 grids out of original 300 radial points. To cover the whole solid angle in space, we use the same uniform 32 grids for azimuthal coordinate while different (non-uniform) 64 grids are used for polar coordinate according to our scheme of advection in the Boltzmann equation. The three input quantities are interpolated accordingly along the polar coordinate. Other thermodynamical quantities are derived from a table of the equation of state by Lattimer & Swesty (1991) for the incompressibility of 180 MeV as used in the original simulations.

In Figure 1, we show the profiles of 3D supernova core adopted in the current study. We take snapshots at 100, 150 and 200 msec after the bounce from their 3D simulation. The timing of adopted snapshots correspond to the scene of expanding shockwave from ~ 300 km to ~ 600 km in a non-spherical manner. The revival of shock wave occurs earlier (at ~ 50 ms) due to the neutrino heating and its outward propagation is assisted by efficient heating through the hydrodynamical instabilities. This 3D model leads to a successful explosion.

We display in Fig. 2 the profiles of the 3D supernova core at 150 ms after the bounce by color maps on the xy-plane ($z=0$). The shock wave is located around 400–500 km with an elongated shape toward $\phi \sim 45^{\circ}$ and $\phi \sim 225^{\circ}$ at this timing. The low entropy region

along $\phi \sim 135^\circ$ and $\phi \sim 315^\circ$ corresponds to the down flow of proton-rich matter. Nearly symmetric distributions with a 180° periodic shape arise from the initial perturbation with ϕ -periodicity given in the original 3D simulation (Takiwaki et al. 2012). The density and temperature distributions of the central object (proto-neutron star) are spherical with deformation of outer layers. The shapes on the xy-plane of the supernova cores at the other times show similar deformation but with elongations at different ϕ -angles.

Figures 3 and 4 show the color maps of entropy and mass fractions on the slices with $\phi=51^\circ$ and 141° . Mushroom-like shapes of high entropy regions reflect the convective motion and the associated shock dynamics in 3D. Along the equator, the high entropy region spreads up to the shock front for $\phi=51^\circ$, but there is a narrow channel of low entropy along the equator for $\phi=141^\circ$. The free neutrons are abundant at center inside the proto-neutron star whereas the free protons are abundant at off-center regions where the entropy is high. Those nucleons behind the shock wave act as absorbing material for the neutrino heating.

3. Neutrino distributions

3.1. Density and flux by Boltzmann evaluation

We examine the neutrino distributions and its associated moments obtained for the three snapshots of the 3D supernova core. We mainly display the numerical results for the snapshot at 150 ms after the bounce. The 3D characteristics of the neutrino transfer, which we discuss below, are mostly common also for the other snapshots.

We show in Fig. 5 the iso-surfaces of the density of electron-type anti-neutrinos ($\bar{\nu}_e$) with arrows of its flux vector. The distribution of neutrinos is spherical at center, but deformed in the surrounding region, reflecting the convective high entropy region. The

corresponding fluxes are non-radial according to the gradients of the deformed distributions. The distribution further out is again spherical due to the outward neutrino fluxes at large radii. These 3D features are seen also for the densities and fluxes for electron-type neutrinos (ν_e) and μ -type neutrinos (ν_μ).

Figure 6 displays the density of neutrinos for three species (ν_e , $\bar{\nu}_e$ and ν_μ) by color maps on the xy-plane ($z=0$). The ν_e -distribution is focused inside the proto-neutron star at center with high chemical potential of neutrinos. The $\bar{\nu}_e$ - and ν_μ -distributions concentrate in the off-center region, where the degeneracy is low due to high entropies. Among the three species, the $\bar{\nu}_e$ -distribution exhibits the most non-spherical feature. The ν_e -distribution is spherical at center and slightly deformed in the surrounding region. They are affected by the non-spherical shape of the degeneracy of neutrinos ($\eta_\nu = \mu_\nu/T$). The ν_μ -distribution is entirely spherical, reflecting the spherical shape of temperature distribution as seen in Fig. 2.

The 6D Boltzmann solver handles the advection in 3D space and, therefore, describes the non-radial advection as well as the radial advection. Figure 7 reveals the three components of the flux of $\bar{\nu}_e$ on the xy-plane ($z=0$) corresponding to Fig. 6. There are significant contributions of polar (θ) and azimuthal (ϕ) fluxes due to the deformed $\bar{\nu}_e$ -distribution. The direction of the flux follows roughly the gradient of neutrino distribution in the central region. We stress that non-uniform azimuthal fluxes are described properly in the 6D Boltzmann solver by removing the axisymmetric assumption. The size of the non-radial component of the flux reaches more than 50 % of the radial component around 20–50 km inside the proto-neutron star. The non-radial fluxes persist up to larger radii though they become smaller. The neutrino transport is diffusive well inside a radius of 50 km and transitional to free streaming toward 100 km. As we will see in Figs. 27 and 29, the second moment of angle, $\langle \mu_\nu^2 \rangle$, is less than 0.35 inside the radius of 50 km so that

the diffusion regime is confined within this radius. The 6D Boltzmann solver enables the seamless description of non-radial flux in the wide region while applicability of the diffusion approximation is limited within the diffusion regime.

Figure 8 show the neutrino densities for three species on the slice of $\phi=51^\circ$ and 141° in the central region. The deformed shapes of density distributions are seen for ν_e and $\bar{\nu}_e$ while the shape is spherical for ν_μ . The $\bar{\nu}_e$ and ν_μ are abundant at the off-center region due to their origin of thermal production. The former reflects the neutrino degeneracy in addition to the character of high entropy. There is a bump around the equator in the case of $\phi=141^\circ$ for ν_e and $\bar{\nu}_e$. This corresponds to the narrow channel of the proton-rich and low entropy condition seen in Fig. 4. The production of neutrinos is amplified by local enhancement of thermodynamical quantities, which we discuss later.

Prominent non-radial fluxes of ν_e and $\bar{\nu}_e$ can be seen in Figs. 9 and 10, where three components of fluxes are shown. The polar component exhibits fine structure with alternating directions and the azimuthal components widely extends. It is remarkable to see that the directions of flux for ν_e and $\bar{\nu}_e$ are opposite each other. This is because the neutrino chemical potential and temperature (and their gradient) affect the distributions of two species in a opposite way. (See Fig. 11 and discussion below) The flux for ν_μ is almost spherically symmetric (not shown here) and its radial flux concentrate around its off-center density distribution. The magnitude of the non-radial fluxes is comparable to that of radial flux in some regions. Its ratio reaches more than 50 % around the central object up to $r \sim 40$ km. The fluxes extend up to 100 km for ν_e in the case of $\phi=141^\circ$. This corresponds to the narrow region along the equator noted above.

In the three snapshots, the neutrino distributions evaluated by the 6D Boltzmann solver are similarly inhomogenous around the central region and rather spherical in the outer part. At center, the proto-neutron star is almost spherical due to the spherical distributions of

density and temperature. Having deformed shape in the profile of electron fraction, though, the distribution of the neutrino chemical potential is non-spherical. We show in Fig. 11 the temperature, neutrino chemical potential and neutrino degeneracy on the ϕ -slices corresponding to Figs. 8, 9 and 10. We overlay the location of the neutrino-sphere of the neutrinos with an energy bin of $E_\nu = 34$ MeV for three species. Here the neutrino-sphere is defined by the location where the optical depth is 2/3 along the radial coordinate. For this purpose, we evaluated the optical depth by using the opacities for the neutrinos in the forward angle bin. While the temperature distribution is almost spherical, the chemical potential (i.e. degeneracy) shows non-uniform feature in the central region inside the neutrino-sphere and the surrounding region up to the location of the shockwave. This leads to inhomogeneous distribution of ν_e and $\bar{\nu}_e$ and spherical distribution of ν_μ . In the outer layers, the neutrino distribution becomes more spherical due to an averaging effect by the integration of neutrino fluxes from various angles. This is the characteristics of the 6D Boltzmann solver to describe the advection in 3D space. This finding is in accord with the result found in 2D space by Ott et al. (2008) through comparisons with the diffusion approximations. We will demonstrate different characteristics in the ray-by-ray approximation through comparisons with the 6D Boltzmann results in the following sections.

The deviations from the spherical shape even in the outer layers occur in the case of $\phi=141^\circ$ due to a spot in the narrow channel along the equator. In this region, the neutrino-spheres of ν_e and $\bar{\nu}_e$ pass through the degenerate regime, i.e. low temperature and high neutrino chemical potential. This spot effect is evident in densities and fluxes for ν_e , modest for $\bar{\nu}_e$ and not discernible for ν_μ . This order corresponds to the positions of neutrino-sphere for three species in depth toward the center. In the case of $\phi=51^\circ$, variations of neutrino degeneracy around the neutrino-spheres are not drastic, therefore, leading to rather spherical distributions in the outer layers besides non-uniform distributions

at center. We see these two types of behavior in non-uniform situations depending on the slices and the timing in the three snapshots we have studied. The spot effect may cause enhanced/reduced neutrino distributions and associated change of heating rates as we will examine below.

3.2. Density and flux by ray-by-ray evaluation

In this section, we demonstrate that the neutrino distributions evaluated by the ray-by-ray approximation exhibit the enhanced non-spherical shape by reflecting the internal environment. We compare the results with the full 6D Boltzmann evaluation to extract the characteristics of the ray-by-ray approximation. We also evaluate the size of deviation of the neutrino distributions between the two methods. The deviation of the quantity, δ_Q , is hereafter defined by $\delta_Q = (Q_{RbR} - Q_{Boltz})/Q_{Boltz}$, where Q_{RbR} and Q_{Boltz} are the values obtained by the ray-by-ray and Boltzmann evaluations, respectively.

The neutrino densities by the ray-by-ray approximation retain non-spherical feature in outer regions, being different from the spherical shape obtained in the 6D Boltzmann evaluation. In the central region, the two methods provide the same non-spherical distributions since the neutrinos are trapped well inside the diffusion regime. In Fig. 12, we display the profiles of neutrino densities for ν_e and $\bar{\nu}_e$ obtained by the two methods on the xy-plane. The deviation of the ray-by-ray evaluation with respect to the 6D Boltzmann evaluation is also shown in the bottom panels. The distribution is not spherical even for the outer region (> 100 km) in the ray-by-ray evaluation. This is caused by the enhancement of anisotropy due to the ray-by-ray approximation. The neutrino fluxes are mainly determined by the environment at the neutrino-sphere. In the ray-by-ray approximation, the enhancement (or reduction) of neutrino fluxes due to variations of temperature and chemical potential around the neutrino-sphere are kept along the specific

radial ray. Therefore, the overestimate (or underestimate) of neutrino densities appears depending on the direction of rays as shown in the bottom panels.

The same feature can be consistently seen in the behavior of fluxes shown in Fig. 13. The distributions of fluxes in the ray-by-ray approximation have non-spherical feature in the outer region due to enhancement or reduction depending on the direction. In some directions, the deviation of ν_e flux has anti-correlation with that of $\bar{\nu}_e$ flux. When the neutrino chemical potential is high at the neutrino-sphere in one ray, the ν_e flux is enhanced along the ray but $\bar{\nu}_e$ flux is suppressed. Although the neutrino fluxes for two species may depend on the location of neutrino-spheres, the environment and other factors, we find that this feature often appears in many profiles of our samples as we will show.

We demonstrate that the anisotropy in the ray-by-ray approximation can be large enough to affect the densities and fluxes at large distances, depending on the slice. Fig. 14 shows the neutrino densities obtained by the ray-by-ray approximation on ϕ -slices, which corresponds to the ones in Fig. 8. The neutrino densities of ν_e and $\bar{\nu}_e$ are not spherical at ~ 100 km in contrast to the spherical shape found in the 6D Boltzmann evaluation. In the case of $\phi=141^\circ$, the anisotropy around the equator is enhanced more than that in the 6D Boltzmann evaluation. We display the deviation of the ray-by-ray evaluation in Fig. 15. Because of the enhancement (or reduction) at the emission region, the influence persists due to the averaged radial propagation of neutrinos along the ray. Depending on the polar direction, there are regions of overestimate or underestimate of densities for ν_e and $\bar{\nu}_e$ in the outer region. There is anti-correlation of deviations between the two species (ν_e and $\bar{\nu}_e$) depending on the ray. This is again because the emission is determined by the neutrino degeneracy, which enhances and reduces the flux of ν_e and $\bar{\nu}_e$, respectively.

The anisotropy of densities arises from angular dependence of the fluxes of neutrinos emitted from the region of neutrino spheres. We show the behavior of neutrino fluxes in

Figs. 16 and 17 for the two slices at $\phi=51^\circ$ and 141° , respectively. The deviations of the ray-by-ray evaluation from the 6D Boltzmann evaluation are also displayed for each profile in the right panels. One can clearly see the overestimate or underestimate of the fluxes along the ray, depending on the polar angle. The anti-correlation between the two species appears apparently on the two slices as seen in the profiles on the xy-plane in Fig. 13. The pattern of deviation in the flux corresponds to that in the densities shown in Fig. 15. In the case of $\phi=141^\circ$, the deviations are large for both species in a wide region. The region around the equator has a significant deviation due to the narrow channel.

We further examine the variations of the neutrino distributions and the anti-correlation between the two species. We show the polar angle dependence of quantities at the fixed radius on the slice of $\phi=51^\circ$ in Figs. 18 and 19. The neutrino densities are well determined by the local environment (temperature and neutrino chemical potential) in the diffusion regime at radius of 54 km in Fig. 18. We see the neutrino densities follow the variation of the neutrino chemical potential while the anti-neutrino densities have the anti-correlated variation. μ -type neutrinos have a constant distribution since the temperature stays almost constant. Both the two evaluations provide the neutrino distributions simply reflecting the environment. The ray-by-ray evaluation shows slightly stronger variations than the 6D Boltzmann evaluation.

Neutrino distributions become different from the variation of local environment as we leave the diffusion regime and go further away from the region of the neutrino-sphere. At radius of 94 km in Fig. 19, the neutrino densities by the 6D Boltzmann evaluation become more flat than the variations in the neutrino chemical potential. This is due to the averaging effect by the non-radial fluxes. In contrast, the neutrino densities by the ray-by-ray evaluation show clear variations due to the degeneracy, keeping the anisotropy made deep inside the core. The anti-correlation between the two species remains similar

to the situation at the inner position in the two evaluations. As shown in these examples, the non-uniform distribution of neutrino chemical potential inside the core is important to determine the neutrino distributions in the outer region. Note that the electron fraction is an important factor to determine the neutrino chemical potential when the distributions of density and temperature are spherical inside the core.

4. Evaluation of energy transfer rates

We examine the evaluation of heating rate in the supernova core by using the collision term in the 6D Boltzmann equation. Since the heating rate is a crucial quantity to explore the neutrino heating mechanism, one has to carefully determine the size of the heating rate in multi-dimensional distributions of material. We investigate the heating rate obtained by the ray-by-ray method so that we can assess possible errors in the popular approximation currently used to explore explosions combined with hydrodynamical instabilities. We show that deviations of the heating rate along the ray occur due to the ray-by-ray approximation in some directions and snapshots. The size of deviation depends on the environment inside the core, which provides the deviations in neutrino densities and fluxes we have seen in the previous sections.

4.1. Heating rate by Boltzmann and ray-by-ray evaluations

We describe here the behavior of the heating rates in the supernova core at 150 msec after the bounce by the two methods. We display the heating rates on the xy-plane in Fig. 20 by the 6D Boltzmann (top) and ray-by-ray (middle) evaluations. The relative deviations of the ray-by-ray approximation with respect to the 6D Boltzmann evaluation are also shown in the bottom panel. While we see mostly similar profiles of heating region

in red, there are two spots with enhanced heating rates in the ray-by-ray evaluation shown in the middle panel. Along the two directions, there are overestimates of ~ 0.2 in the ray-by-ray approximation. This enhancement corresponds to the enhanced densities and fluxes seen in Figs. 12 and 13. The deviation arises from the inhomogeneous distributions of neutrino degeneracy, which act like a *hot spot* for neutrino emissions. We can also see minor deviations in some directions. Note that deviations to a certain extent can occur in the central part near the gain region, where the energy transfer rate is very small.

Figure 21 displays the corresponding profiles for the neutrino heating rate on ϕ -slice at $\phi=51^\circ$ and 141° in the same snapshot. The heating rates by the 6D Boltzmann (left) and ray-by-ray (middle) evaluations are shown with the relative deviations of the ray-by-ray evaluation (right). In the case of $\phi=51^\circ$, there is no noticeable difference in the heating rates between the two methods except for a slight underestimation along two directions. Significant deviation with overestimation is seen along the equator in the case of $\phi=141^\circ$. This corresponds to the one of the directions with overestimate seen in Fig. 20. The neutrino heating in the ray-by-ray evaluation is strong along the ray near the equator due to the enhanced neutrino fluxes in the narrow channel. There are also wide regions with overestimate and a direction with underestimation in the heating region.

While the deviations of the *total* heating rate are limited in some directions, those for each heating rate for major reactions generally occur in the whole region. In Figure 22, we show the heating rates and their deviations for ν_e and $\bar{\nu}_e$ absorptions on ϕ -slice at $\phi=51^\circ$. One can see local enhancement or reduction of the heating rate by the ray-by-ray evaluation from that by the 6D Boltzmann evaluation. On the one hand, significant deviations with alternate sign appear depending on the ray direction for the ν_e absorption in the upper panel. This pattern arises from the deviations of ν_e fluxes and reflects the pattern seen in Fig. 16. On the other hand, deviations of the similar size for the $\bar{\nu}_e$ absorption appear

in the same pattern but with a different sign. This pattern reflects the corresponding pattern for $\bar{\nu}_e$ in Fig. 16. Due to the mechanism of the deviation in fluxes for two species, the overestimate and underestimate of the heating rates can arise in the opposite way. Therefore, the total heating rate does not have large errors in most of the directions due to cancellation of the two deviations. This mechanism of the cancellation of the two heating rates, which have sizable deviations with different signs, is generally seen on many slices in the other profiles at different timings.

The anisotropy of heating rate depending on the direction in the ray-by-ray approximation may have influence on the local structure and motion in multi-dimensions. The enhancement of heating beamed along a certain direction may lead to the modification of dynamics on the particular region. In contrast, the 6D Boltzmann evaluation provides mildly anisotropic distributions of the neutrino heating by the integration from various angles. We remark here that the anisotropy in the ray-by-ray approximation is found in the fixed hydrodynamics. It is necessary to examine whether this feature persists for a long time scale in dynamical situations by neutrino-radiation hydrodynamics.

4.2. Heating rates in other profiles

We investigate the heating rates in the other profiles at different timings to explore general characteristics of the 6D Boltzmann and ray-by-ray evaluations. We demonstrate that appreciable deviations of the ray-by-ray approximation occur along the radial ray in the other snapshots. Their magnitude and sign vary depending on polar and azimuthal directions in each case.

The heating rate by the 6D Boltzmann evaluation and the relative deviation by the ray-by-ray approximation at 100 ms after the bounce are shown in Figs. 23 and 24. One

can see, in Fig. 23, the deformed shape of the heating region and the underestimation of the heating rate widespread on the xy-plane with a fluctuating size. In Fig. 24, the overestimation of the heating rate occurs around the z-axis within a wide polar angle while the underestimation is confined on the equator. In this snapshot, the neutrino heating is enhanced along the polar directions in the ray-by-ray approximation. The heating rate in the ray-by-ray evaluation is higher around the polar axis and lower on the equator independent of ϕ -direction than the corresponding evaluation by the 6D Boltzmann solver.

The behavior is different in the case of the profile at 200 msec in Figs. 25 and 26. The underestimation and overestimation alternately occur in the ϕ -direction on the xy-plane as seen in Fig. 25. Depending on the polar angle, there are large variations of the deviation on the ϕ -slice in Fig. 26. In the case of $\phi=51^\circ$, the limited region of underestimation appears with large magnitude along a certain direction. In the case of $\phi=141^\circ$, there is significant overestimation focused along a particular polar direction. The deviations in other polar directions are rather moderate. This beam-like structure resembles the case of $\phi=141^\circ$ at 150 msec. In fact, the neutrino degeneracy around the neutrino sphere is locally high at two spots, which lead to high neutrino fluxes and, therefore, heating rates. These spots are located around a narrow channel between the two mushroom-like flows like the case for 150 msec.

4.3. Volume integrated heating rates

Since we found that the heating rates are locally different, it is of great importance to examine the total amount of the heating rate in the two evaluations. We evaluate the volume integrated heating rates by the 6D Boltzmann solver and the ray-by-ray approximation to check this point. The specific heating rates, on which we have discussed

in the previous sections, are defined by

$$q_\nu = - \int d\Omega E_\nu^2 dE_\nu E_\nu \left(\frac{\delta f}{\delta t} \right)_{collision}, \quad (1)$$

with the collision term in the Boltzmann equation. The total amount of the heating rate is calculated by the integral over the volume in the heating region,

$$Q_\nu = \int dV q_\nu \rho, \quad (2)$$

where ρ is the mass density. The range of the integral covers the heating region, where the energy transfer is positive. We identify the inner boundary of the heating region as the gain radius, where $q_\nu = 0$ along the radial coordinate. We adopt the outer boundary as the location of the shock wave when the entropy per baryon becomes 5.5 in the unit of the Boltzmann constant, k_B .

In Table 1, we compare the volume integrated heating rates in the two evaluations. The volume integrated heating rates in the ray-by-ray approximation are slightly smaller than the values in the 6D Boltzmann evaluation, but the deviation is within $\sim 2\%$. One may wonder the reason why the volume integrated heating rate by the ray-by-ray approximation is not significantly different from the one by the 6D Boltzmann solver. This is because the deviations in the local heating regions cancel out by the integral over directions having both overestimation and underestimation depending on the ray. The current analysis suggests that the local deviations in the ray-by-ray approximation are more significant than the total deviations. It should be noted, however, that even a slight deviation in the total heating rate can be crucial to the revival of the shock wave in the marginal situation (Janka & Müller 1996). It is necessary to study this influence further by examining other timings and its time duration.

5. Angle moments

Various moments of the neutrino distribution are important to reveal the feature of the neutrino transfer in 3D space. They are also useful to develop new methods for the closure relation in the moment formalism (see Shibata et al. (2011) for example). In principle, we can derive various moments of angle and energy from the obtained neutrino distribution in six dimensions. As an example, we show the contour maps of the angle moments of the neutrino distributions for three species in Figs. 27 and 29 on the slice at $\phi=51^\circ$ and $\phi=141^\circ$, respectively, for the 3D supernova core at 150 ms after the bounce. The distributions of both the flux factor, $\langle\mu_\nu\rangle$, and the second moment of angle, $\langle\mu_\nu^2\rangle$, are almost spherical with slight deformation in the central part. Some bumps are seen around the narrow region along the equator on the slice of $\phi=141^\circ$.

We further examine the angle moments obtained by the ray-by-ray approximation through comparisons with the 6D Boltzmann evaluation. In Figs. 28 and 30, we show the relative deviations of the angle moments evaluated by the ray-by-ray approximation with respect to the 6D Boltzmann evaluation. Appreciable deviations of the angle moments arise in some regions where there are large non-radial fluxes in the neutrino distributions. The size of deviations becomes large up to $\sim 10\%$ corresponding to the size of deviations in the other quantities we have seen. The deviations are very small within $\sim 3\%$ for $\langle\mu_\nu^2\rangle$ on the slice of $\phi=51^\circ$ where the distribution is almost spherical. On the slice of $\phi=141^\circ$, the deviation is significant around the narrow channel on the equator due to the hot spot effect. We see alternate deviations (underestimate and overestimate) along the radial ray due to the ray-by-ray approximation.

It is profitable to note that we can examine all (diagonal and non-diagonal) elements of the Eddington tensors obtained by the 6D Boltzmann solver. Components of the Eddington tensor reflect interesting features with non-spherical shapes in some cases. The diagonal

elements of the Eddington tensor for the energy bin ($E_\nu = 34$ MeV) of two species of neutrinos (ν_e and $\bar{\nu}_e$) are shown in Figs. 31 and 32 on the two ϕ -slices for the snapshot at 150 ms. In the case of $\phi=51^\circ$, the distributions of the three components exhibit deformed shapes in the outer region (~ 250 km). In the central part, they have spherical shape for ν_e and non-spherical one for $\bar{\nu}_e$, reflecting their distributions. In the case of $\phi=141^\circ$, the non-spherical feature of the distribution is prominent in a wide region for the two species. The bumpy structure reflects the shape of the supernova core, which has the narrow channel between the two mushrooms along the pole.

In usual situations close to spherical situation, only the diagonal elements are dominant with non-zero contributions. We found that there are some regions where the non-diagonal elements are non-zero. In Fig. 33, we show, as an example, the contour map of the non-diagonal $(r\theta)$, $(r\phi)$ and $(\theta\phi)$ -components for the energy bin ($E_\nu = 34$ MeV) of ν_e on the slice of $\phi=141^\circ$ in the case of 150 ms. Their size amounts to ~ 0.1 and is not negligible around the channel along the equator.

These non-trivial properties of the Eddington tensors are valuable information to examine the anisotropy of neutrino distributions from the 6D Boltzmann solver. Since the neutrino distribution is symmetric around the radial coordinate in the ray-by-ray approximation, only the three diagonal components are non-zero. In addition, the rr -component determines the other two $\theta\theta$ and $\phi\phi$ -components. Hence, the ray-by-ray approximation loses the information of the non-trivial structure of the Eddington tensor. Further studies on the detailed behavior of the Eddington tensors obtained by the 6D Boltzmann solver are underway to develop new closure relations for the 3D problems as a separate article.

6. Discussions

We discuss here implications on the supernova mechanism and associated phenomena based on the characteristics of the neutrino transfer obtained by the 6D Boltzmann solver and the ray-by-ray approximation.

The 6D Boltzmann solver provides a seamless description of the neutrino transfer in 3D space. Non-radial neutrino transfer appears in general and can prevail up to large distances. The 3D transport of neutrinos can have influence on convective motion of neutrino-rich matter inside the proto-neutron star as well as emission properties around the neutrino sphere in 3D hydrodynamics. These outcomes may in turn affect the neutrino heating mechanism for the revival of shock wave.

Although the diffusion approximation can describe the non-radial transfer of neutrinos in the diffusion regime, the transition to the transparent regime is handled by prescribed form of the flux limiter. The non-radial neutrino flux at large distances outside the diffusion regime, which we have seen in the examples, can not properly described by the diffusion approximation. The flux in the intermediate regime, being different from the one determined by the local gradient, may have impact on the surrounding region in a non-local manner. The 6D Boltzmann treatment is a unique solution to describe such circumstances. It is desirable to study the consequence of such effects by performing the neutrino-radiation hydrodynamics.

The study of the evaluation by the ray-by-ray approximation through the comparison with the 6D Boltzmann evaluation is beneficial for the supernova studies using the ray-by-ray approximation. This approximation is routinely used for the state-of-the-art numerical simulations in 2D and 3D spatial dimensions. Our evaluation by the ray-by-ray approach based on the same Boltzmann equation is suitable to gauge the influence of the approximation. While the ray-by-ray approach is an efficient way to handle the neutrino

transfer in multi-dimensions, it is inevitably lacking the ability to describe fully the non-radial neutrino transport (See Buras et al. (2006) for partial coupling). It also tends to enhance the directional variation of the neutrino variables such as density, flux and luminosities for the fixed backgrounds in 3D space. This feature found by the 6D Boltzmann solver is in accord with the result in the 2D supernova cores through comparisons with the diffusion approximation by Ott et al. (2008) and Brandt et al. (2011). It remains to be seen if this effect persists in dynamical situations.

If the enhancement of neutrino anisotropy lasts for a long period, it may have impact on the hydrodynamics through the interaction of neutrino-radiation and hydrodynamics. For example, a large neutrino heating rate along a certain direction may cause strong push to the stalled shock wave locally. Opposite situation with small heating and shrinkage of shock wave can arise in another direction as well. Variations of the heating effect in the ray-by-ray approximation, therefore, may enhance deformation of the shock wave and might induce associated hydrodynamical instabilities. In the 6D Boltzmann treatment, such angle-dependent effects are smoothed out by the global integration of fluxes from many directions. It is advisable to make detailed studies on the anisotropy of neutrino variables due to the local inhomogeneity of environment with attention to the treatment of neutrino transfer.

From our evaluation, the size of deviation due to the ray-by-ray approximation is moderate for most of the profiles except for some significant cases. This may be helpful information for the studies using the ray-by-ray approximations to explore the supernova dynamics in 3D, since the supercomputing resources are limited to allow the detailed 3D simulations with microphysics only by approximate treatment of neutrino transfer at present. In future, however, it is necessary to perform the 3D hydrodynamics with the 6D Boltzmann equation to remove the uncertainty due to the neglect of non-radial flux

and the averaging effects on the directional anisotropy. Even with a small deviation of the heating rate of $\sim 10\%$ may have an impact on the revival of the shock wave when the dynamical situation is marginal. Our investigation aims to evaluate the magnitude of influence induced by the approximations and to develop the numerical method to remove the current restriction of the neutrino transport.

The 6D Boltzmann solver opens up new possibilities to study the signal of neutrino bursts from the 3D supernova cores. The current approach enables us to obtain the spectra of neutrino emission at the boundary for all directions. The neutrino distribution is determined by the integral of contributions from the neutrino fluxes along many directions. The neutrino spectra reflect properties of wide surface area of the emitting object at center. The ray-by-ray approximation, in contrast, the neutrino spectra is determined along the particular ray. The neutrino signal in this approximation may have strong directional dependence on the local conditions of the surface. It is also interesting to examine influence on the nucleosynthesis of heavy elements via the neutrino process through the modification of neutrino spectra.

The approach to solve the Boltzmann equation is able to see the directional dependence of neutrino signal due to the deformation of the central object. When the proto-neutron star is strongly deformed due to the rapid rotation, for example, the subtended area is different between the pole and the equator. The resulting fluxes are different depending on the surface areas from the viewing angle. Such an effect is pointed out by Ott et al. (2008) in the case of a rapidly rotating 2D supernova core. The observational aspect of the directional variations in 2D has been studied by the S_n method (Brandt et al. 2011). In the 3D profiles we have studied, the directional dependence is not strong since the central core is not significantly deformed. Further studies are necessary to explore possible effects on the neutrino signals in the 3D supernova cores by the 6D Boltzmann approach.

The current approach to solve the Boltzmann equation has its limitation on angular resolution for description of forward-peaked neutrinos due to the usage of the S_n method. The fixed angular mesh for neutrino directions in the S_n method requires a large number of grids to obtain the angle resolution at large distances. In the current study, we mainly concern the heating region, which is rather close to the central neutrino-emitting object. In this case, the moderate angular resolution is sufficient to describe distance contrast between 50 km to 500 km, for example.

If one requires the detailed neutrino spectra at the surface of a Fe-core (~ 5000 km, for example), one needs a more fine angular mesh, especially, to describe them with variations of thermodynamical conditions at the surface of proto-neutron star. The increase of the number of angular grids, however, requires prohibitive computing resources since the computational load to solve dense block matrices for angle coupling becomes further expensive. (See §4 in Kotake et al. (2012) for the scaling of computational load.) It will be necessary to develop a numerical method with alternative techniques such as the variable angle mesh (Yamada et al. 1999), the tangent ray method (Stone et al. 1992), or the Monte Carlo method (Abdikamalov et al. 2012).

Since the current study is limited to the three snapshots from a particular 3D supernova simulation, it would be desirable to study the neutrino transfer in various snapshots at different situation of the shock wave. These include variants of position, shape of deformation of the shock wave as well as the degree of stall. The current model is taken from the 3D simulation which leads to a successful explosion in a rather short time period. It is more crucial to see whether the 3D neutrino transfer is influential when the shock wave stalls and waits for a long period for the revival. It remains to examine the sequential profiles over the hydrodynamical time scale in order to check whether the angle variations due to the ray-by-ray approximation persist. If the directional fluctuations

of the heating rate lasts for a long period, they firmly affect the hydrodynamics and its subsequent evolution of the shock wave. The amount of the total heating integrated for a certain period is important for the overall dynamics for the explosion.

It is profitable to study further the neutrino transfer in 3D space for various snapshots of other progenitors and scenarios in order to extract the common properties and to find new feature in the 6D Boltzmann evaluation. It is also interesting to perform the 6D Boltzmann evaluation in rotating supernova cores, which bring the global neutrino anisotropy depending on the angle in addition. Numerical studies of the neutrino transfer in the collapsar with a rotating disk, which originates from more massive stars, are important to explore the neutrino heating for the jet formation as a model of the gamma ray burst. Studies on the moments of neutrino angular distributions in such profiles are helpful to develop the closure relation for the moment formalism. These aspects are now under investigation with the 6D Boltzmann solver to clarify many aspects of the death of massive stars.

7. Summary

We explore the basic properties of the neutrino transfer in 3D supernova cores by solving the Boltzmann equation in 6 dimensions (3 in space and 3 in neutrinos). We perform the numerical simulations to obtain the stationary distribution of the neutrinos in 6D phase space for fixed backgrounds of the 3D supernova core. We selected the three profiles of the supernova core taken from the 3D supernova simulations by Takiwaki et al. (2012). By adopting the numerical code to solve the Boltzmann equation in 6D, we follow the time evolution of the neutrino distributions until we get the stationary state. The numerical code handles the neutrino transfer in multi-energy and multi-angle group for three neutrino species. The three dimensional propagation of neutrinos is described by the discretization

of the Boltzmann equation by the S_n method. The standard set of neutrino reactions is implemented in the collision term together with the table of equation of state.

This is the first application of the numerical code of the 6D Boltzmann solver to realistic 3D supernova cores. The solution of the 6D Boltzmann equation directly provides the energy and angle distributions of neutrinos in the whole region of the 3D supernova cores. Most importantly, the transport of neutrino in 3D space dimensions is described in the multi-angle description including the non-radial direction. We demonstrate that the 6D Boltzmann solver describes the basic feature of neutrino transfer in 3D space beyond the approximations often used in the current simulations. The azimuthal propagation is described properly for the first time as well as the polar propagation. The numerical results show that the non-radial transport is generally seen inside the proto-neutron star and can extend over the wide region beyond the diffusion regime.

We found that the ray-by-ray approach, which is a popular approximation in the current supernova simulations, provides enhanced directional dependence in neutrino distributions. We study the neutrino transfer in the ray-by-ray approximation for the same 3D snapshots by using our numerical code without the non-radial transport terms. We examine the behavior of the ray-by-ray approximation through the comparison with the evaluation by the full 6D Boltzmann solver. In the ray-by-ray approximation, the non-spherical profiles of neutrino densities and fluxes tend to prevail from center to large distances. This is in marked contrast to the 6D Boltzmann evaluation in which the integral from many directions provides the averaged spherical distribution outside the proto-neutron star. The non-spherical distributions inside the proto-neutron star in the diffusion regime are equally well described in the two evaluations.

Our analysis shows that the ray-by-ray evaluation provides noticeable overestimate or underestimate of densities and fluxes along the radial ray. By examining the deviation

of the ray-by-ray evaluation with respect to the 6D Boltzmann evaluation, we found that the deviations of $\sim 20\%$ develop along the radial ray depending on the direction. Once the neutrino emission is enhanced due to a local hot spot of the neutrino chemical potential, this modification continues along the radial ray. The reduced neutrino emission is similarly maintained along the ray. Therefore, we find alternate distributions of rays of underestimate and overestimate outside the proto-neutron star. This behavior of deviations is seen commonly for ν_e and $\bar{\nu}_e$ distributions, which reflect the non-uniform distribution of the neutrino degeneracy. The sign of the deviations for the two species is opposite each other because of the opposite effects on the emission through the degeneracy.

We show that the heating rates evaluated by the ray-by-ray approximation have moderate deviations along the radial ray depending on the direction. The deviations from the 6D Boltzmann evaluation amount to $\sim 20\%$ in some limited regions and smaller than the deviation of the density and flux. This is because the overestimate and underestimate of the heating rates by ν_e and $\bar{\nu}_e$ cancel each other due to their opposite deviations in many cases. There are regions of significant deviations in the snapshot where the neutrino degeneracy is prominent from the average distribution due to the narrow channel between the two mushroom-like outflows. This hot spot provides the origin of the enhanced heating rate along the particular radial ray, which may locally affect the hydrodynamics. We find that the total amount of heating in the whole heating region in the ray-by-ray evaluation is slightly smaller than that in the 6D Boltzmann evaluation. Our study provides the magnitude of those fluctuations due to the ray-by-ray approximation and calls for careful assessment of the angle-dependent heating effects on the hydrodynamics. We remark that these features are found in the fixed background profiles. Further studies are necessary to examine the effects in variable situations of hydrodynamics.

We illustrate the basic feature of the angle moments and the Eddington tensor in

the 3D supernova cores. We show that the angle moments of the neutrino distributions obtained by the 6D Boltzmann solver have rather spherical profiles. The relative deviations of the ray-by-ray evaluation appear in some regions, but limited in the inner part. The components of the Eddington tensor have more deformed profiles in the wide range depending on the snapshot. Since we have neutrino distribution in six dimensions, we can compute all components of the Eddington tensor from the neutrino distributions by the 6D Boltzmann solver. We clarify the behavior of the diagonal elements (radial, polar and azimuthal components) in a separate manner. We demonstrate that there are regions with appreciable non-diagonal components in one of the snapshots as an example. These basic quantities can be used to study the closure relation for the moment formalism in non-trivial 3D matter distributions.

The current study is a step toward the complete treatment of neutrino-radiation hydrodynamics including the full list of neutrino reactions in the general relativistic framework. In this study, we concentrate on the stationary state of the neutrino transfer in the 3D supernova core. It is of great interest how the 6D Boltzmann treatment affects the neutrino heating mechanism together with hydrodynamical instabilities. The coupling of the 6D Boltzmann solver with the hydrodynamics is necessary to explore the dynamical outcome for explosions. Numerical studies of the standing accretion shock instability are currently underway by our numerical code of the neutrino-radiation hydrodynamics developed using the 6D Boltzmann solver. The framework with the special relativistic effects in the collision term will be reported elsewhere (Nagakura et al. 2014).

Acknowledgments

We are grateful to K. Kotake, H. Suzuki for the collaborations on supernova simulations. K. S. thanks to H. Nagakura, W. Iwakami, K. Nakazato, S. Furusawa, Y. Sekiguchi and N.

Ohnishi for collaborative works and profitable discussions. K. S. expresses his thanks to T.-H. Janka, C. Ott and A. Mezzacappa for valuable comments on the numerical methods of neutrino transfer in 2D and 3D. We thank the project of computational science for sparse matrix solvers by A. Imakura and T. Sakurai and the supporting team of HITACHI for tuning the numerical code on SR16000.

The numerical computations in this work were mainly performed on the supercomputers at High Energy Accelerator Research Organization (KEK) under the support of its Large-scale Simulation Program (Nos.12/13-05, 13/14-10). K. S. acknowledges also the extensive usage of the supercomputing resources at Yukawa Institute for Theoretical Physics (YITP) in Kyoto University, The University of Tokyo, and Research Center for Nuclear Physics (RCNP) in Osaka University.

This work is partially supported by the Grant-in-Aid for Scientific Research on Innovative Areas (Nos. 20105004, 20105005) and the Grant-in-Aid for the Scientific Research (Nos. 19104006, 21540281, 22540296, 24244036) from the Ministry of Education, Culture, Sports, Science and Technology (MEXT) in Japan.

This numerical study on core-collapse supernovae using the supercomputer facilities is supported by the HPCI Strategic Program of MEXT, Japan.

REFERENCES

- Abdikamalov, E., Burrows, A., Ott, C. D., Löffler, F., O’Connor, E., Dolence, J. C., & Schnetter, E. 2012, *ApJ*, 755, 111
- Bethe, H. A. 1990, *Rev. Mod. Phys.*, 62, 801
- Bethe, H. A., & Wilson, J. R. 1985, *ApJ*, 295, 14
- Brandt, T. D., Burrows, A., Ott, C. D., & Livne, E. 2011, *ApJ*, 728, 8
- Bruenn, S. W. 1985, *ApJS*, 58, 771
- Buras, R., Rampp, M., Janka, H., & Kifonidis, K. 2006, *A&A*, 447, 1049
- Burrows, A. 2013, *Reviews of Modern Physics*, 85, 245
- Burrows, A., Livne, E., Dessart, L., Ott, C. D., & Murphy, J. 2006, *ApJ*, 640, 878
- Hayes, J. C., Norman, M. L., Fiedler, R. A., Bordner, J. O., Li, P. S., Clark, S. E., ud-Doula, A., & Mac Low, M.-M. 2006, *ApJS*, 165, 188
- Hirata, K., et al. 1987, *Phys. Rev. Lett.*, 58, 1490
- Iwakami, W., Kotake, K., Ohnishi, N., Yamada, S., & Sawada, K. 2008, *ApJ*, 678, 1207
- Janka, H., & Müller, E. 1996, *A&A*, 306, 167
- Janka, H.-T. 1992, *A&A*, 256, 452
- Janka, H.-T., Hanke, F., Hüdepohl, L., Marek, A., Müller, B., & Obergaulinger, M. 2012, *Progress of Theoretical and Experimental Physics*, 2012, 010000
- Janka, H.-T., Langanke, K., Marek, A., Martínez-Pinedo, G., & Muller, B. 2007, *Phys. Rep.*, 442, 38

- Kotake, K., Sato, K., & Takahashi, K. 2006, Rep. Prog. Phys., 69, 971
- Kotake, K., Sumiyoshi, K., Yamada, S., Takiwaki, T., Kuroda, T., Suwa, Y., & Nagakura, H. 2012, Progress of Theoretical and Experimental Physics, 2012, 010000
- Lattimer, J. M., & Swesty, F. D. 1991, Nucl. Phys., A535, 331
- Liebendörfer, M., Rampp, M., Janka, H., & Mezzacappa, A. 2005, ApJ, 620, 840
- Liebendörfer, M., Whitehouse, S. C., & Fischer, T. 2009, ApJ, 698, 1174
- Livne, E., Burrows, A., Walder, R., Lichtenstadt, I., & Thompson, T. A. 2004, ApJ, 609, 277
- Messer, O. E. B., Mezzacappa, A., Bruenn, S. W., & Guidry, M. W. 1998, ApJ, 507, 353
- Nagakura, H., Sumiyoshi, K., & Yamada, S. 2014, Astrophys. J., in preparation
- Nakazato, K., Sumiyoshi, K., Suzuki, H., Totani, T., Umeda, H., & Yamada, S. 2013, ApJS, 205, 2
- Ott, C. D., Burrows, A., Dessart, L., & Livne, E. 2008, ApJ, 685, 1069
- Shibata, M., Kiuchi, K., Sekiguchi, Y., & Suwa, Y. 2011, Progress of Theoretical Physics, 125, 1255
- Stone, J. M., Mihalas, D., & Norman, M. L. 1992, ApJS, 80, 819
- Sumiyoshi, K., & Yamada, S. 2012, Astrophys. J. Suppl., 199, 17
- Sumiyoshi, K., Yamada, S., Suzuki, H., Shen, H., Chiba, S., & Toki, H. 2005, ApJ, 629, 922
- Takiwaki, T., Kotake, K., & Suwa, Y. 2012, ApJ, 749, 98
- Thompson, T. A., Burrows, A., & Pinto, P. 2003, ApJ, 539, 865

Woosley, S. E., Heger, A., & Weaver, T. A. 2002, *Reviews of Modern Physics*, 74, 1015

Yamada, S., Janka, H.-T., & Suzuki, H. 1999, *A&A*, 344, 533

Table 1: Volume integrated heating rates in the heating region are listed in the unit of [erg/s] for the 6D Boltzmann and ray-by-ray evaluations. The total amount of the heating rate is calculated by the volume integration of the specific heating rate, q_ν [erg/g/s], times the mass density, ρ [g/cm³], where q_ν is positive. (See the definition in §4.3.)

Timing	Evaluation	Heating rate [erg/s]
100 ms	6D Boltzmann	6.93×10^{51}
	Ray-by-ray	6.84×10^{51}
150 ms	6D Boltzmann	4.61×10^{51}
	Ray-by-ray	4.53×10^{51}
200 ms	6D Boltzmann	2.68×10^{51}
	Ray-by-ray	2.65×10^{51}

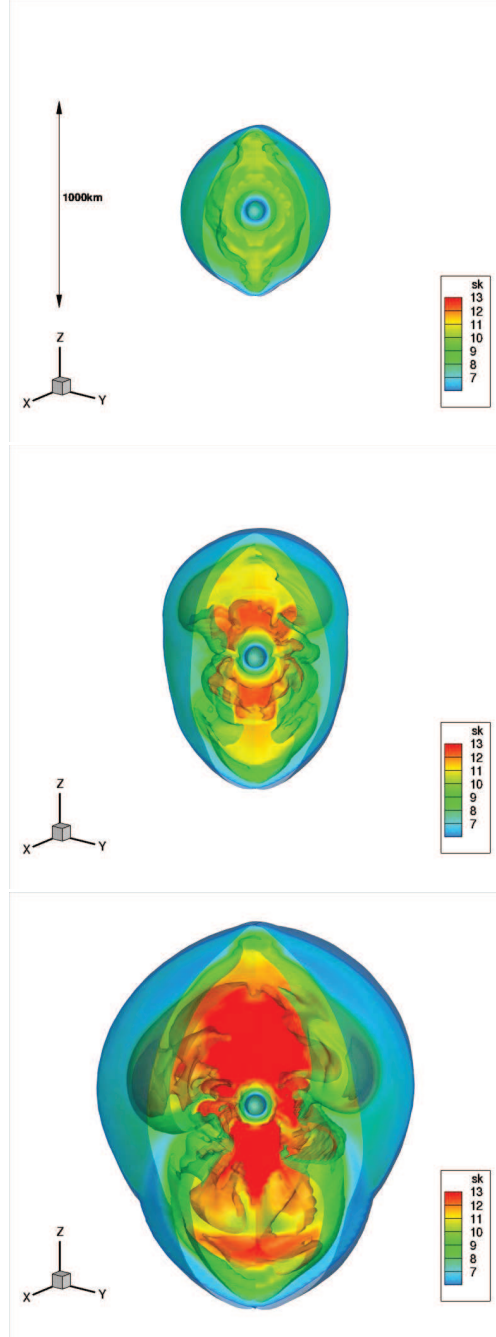


Fig. 1.— Profiles of the 3D supernova core adopted in the current study. Iso-surfaces of the entropy per baryon in the unit of the Boltzmann constant, k_B , are shown for the snapshot at 100, 150 and 200 ms after the bounce in the 3D supernova evolution by Takiwaki et al. (2012) from top, middle and bottom panel, respectively.

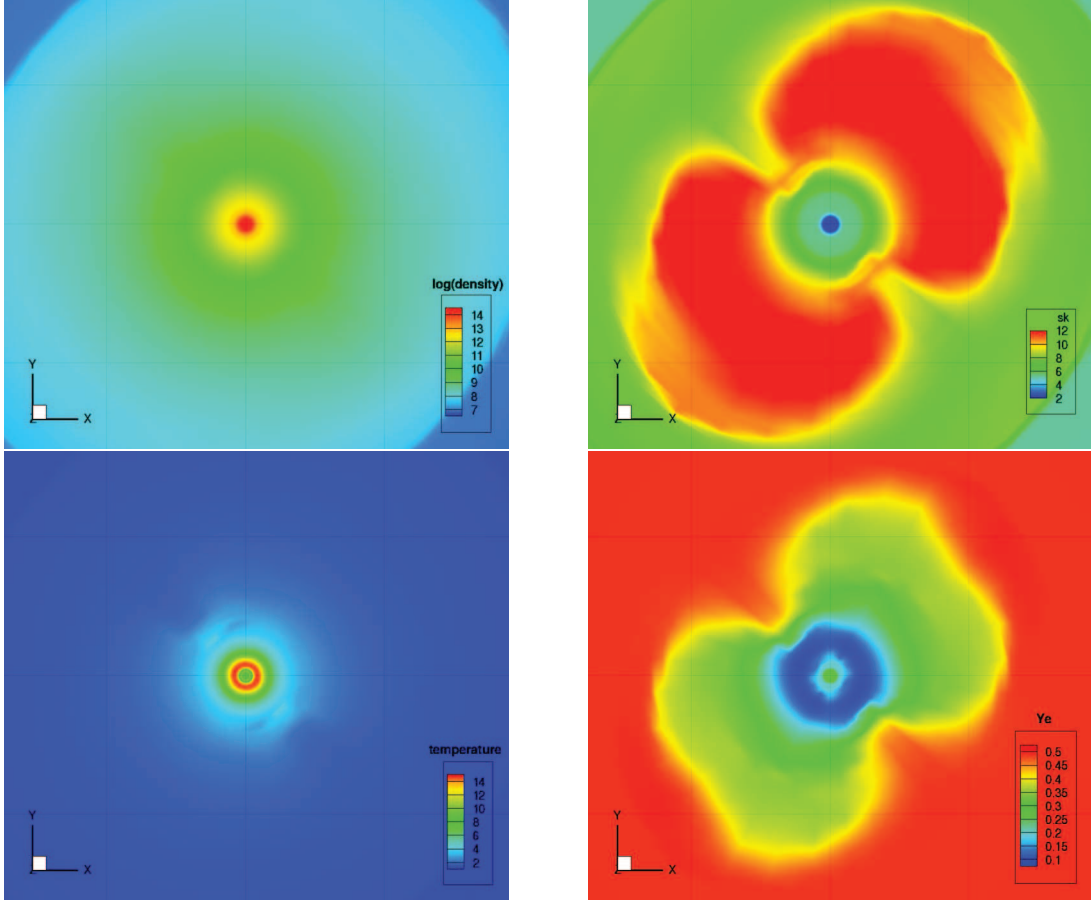


Fig. 2.— Profiles of the 3D supernova core at 150 ms after the bounce are shown on the xy-plane ($z=0$). Density [g/cm^3], entropy per baryon [k_B], temperature [MeV] and electron fraction are plotted by color maps in left-top, right-top, left-bottom and right-bottom panels, respectively. Grid lines with 200 km spacing are shown in the background.

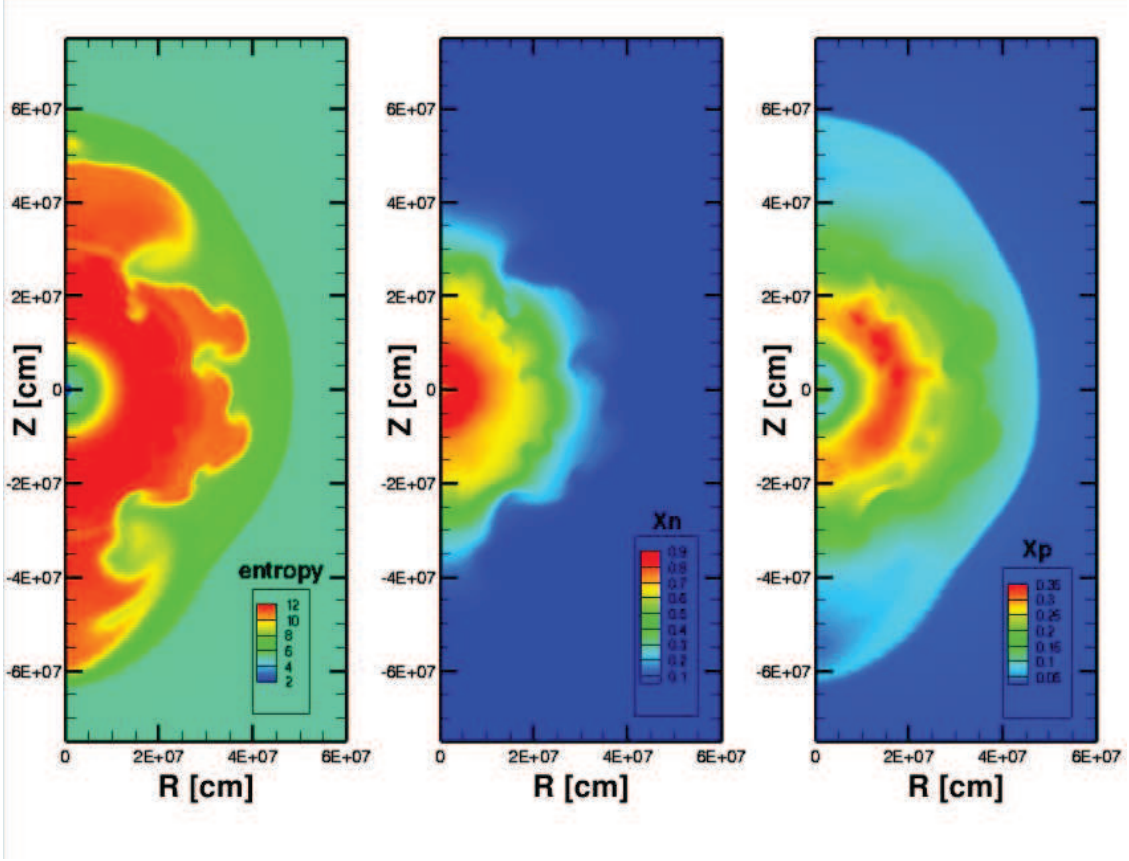


Fig. 3.— Profiles of the 3D supernova core at 150 ms after the bounce are shown on the slices with $\phi=51^\circ$. Entropy per baryon [k_B] and mass fractions of free protons and neutrons are shown by color maps in left, middle and right panels, respectively.

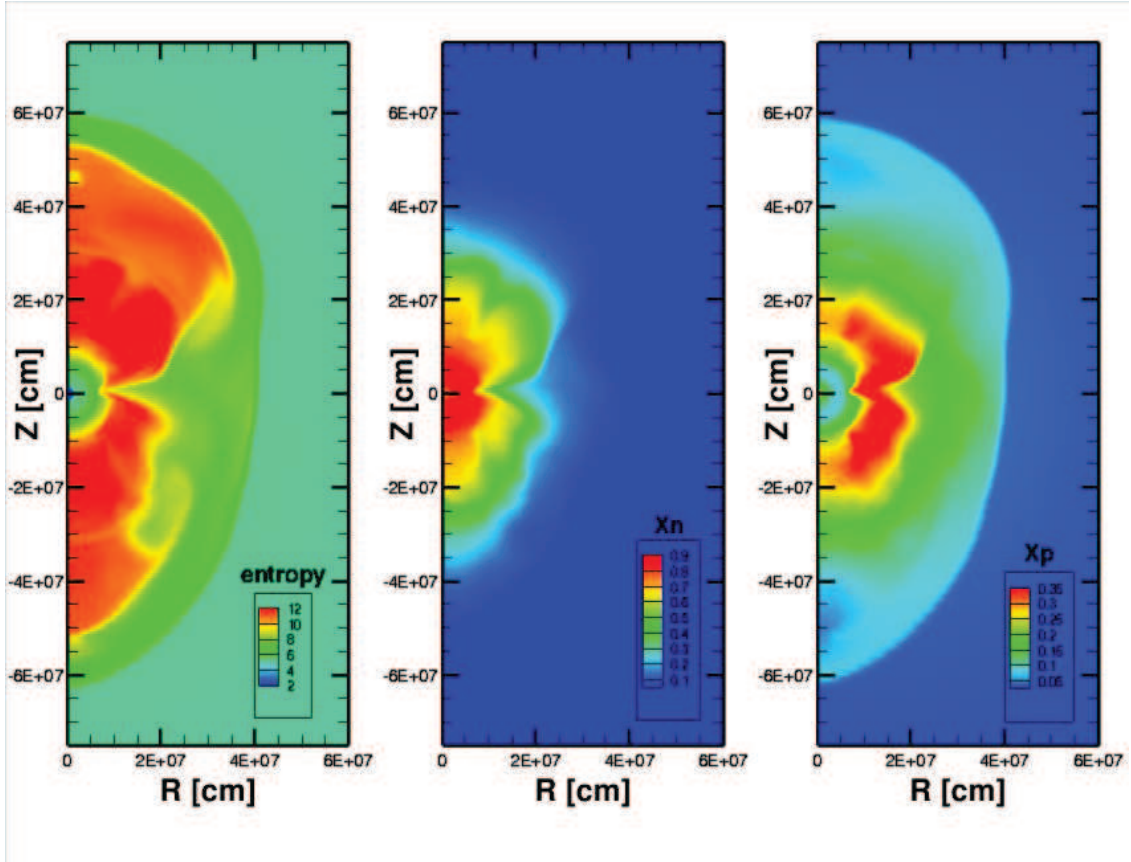


Fig. 4.— Same as Figure 3, but on the slice with $\phi=141^\circ$.

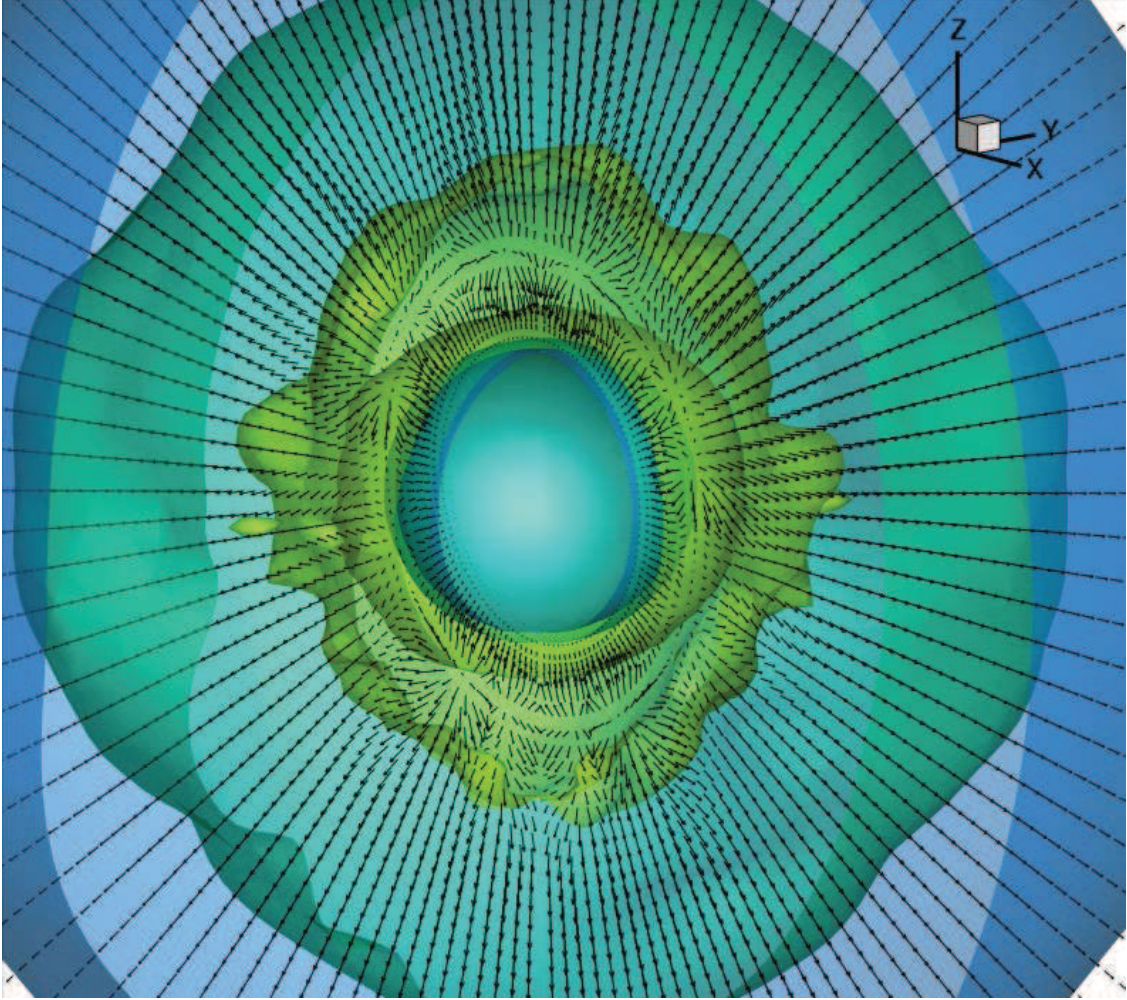


Fig. 5.— Iso-surfaces of density of electron-type anti-neutrinos ($\bar{\nu}_e$) for the 3D supernova core at 150 ms after the bounce. Arrows represent the flux vector of neutrinos.

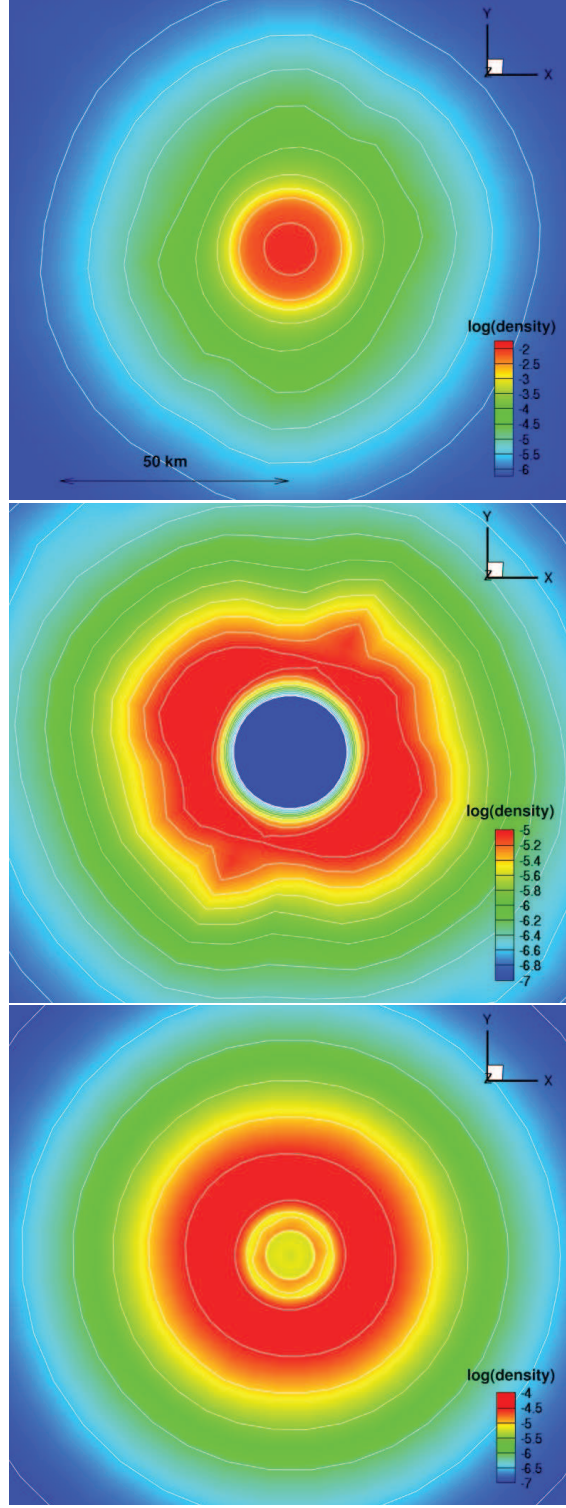


Fig. 6.— Profiles of neutrino density in log scale in the unit of fm^{-3} for three species (ν_e , $\bar{\nu}_e$ and ν_μ) for the 3D supernova core at 150 ms after the bounce are shown by color maps on the xy -plane ($z=0$) in the top, middle and bottom panels, respectively.

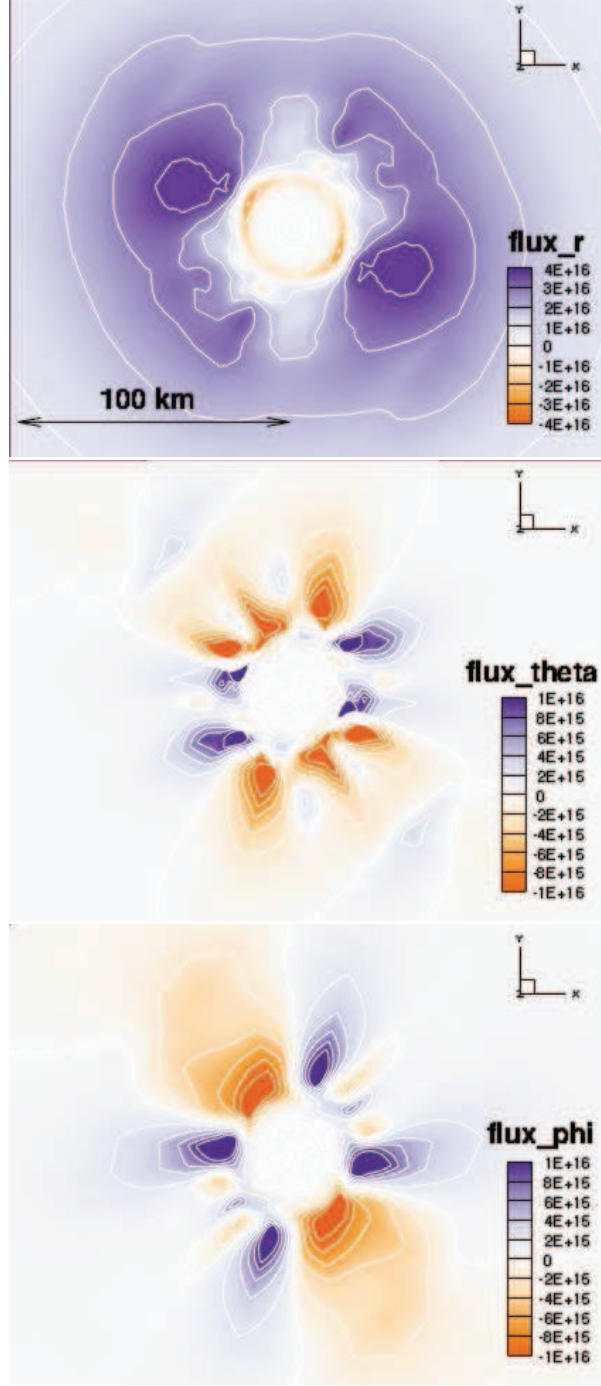


Fig. 7.— Profiles of number flux of $\bar{\nu}_e$ in the unit of $\text{fm}^{-2}\text{s}^{-1}$ for the 3D supernova core at 150 ms after the bounce are shown by color maps on the xy -plane ($z=0$). The radial, polar and azimuthal fluxes are shown in the top, middle and bottom panels, respectively.

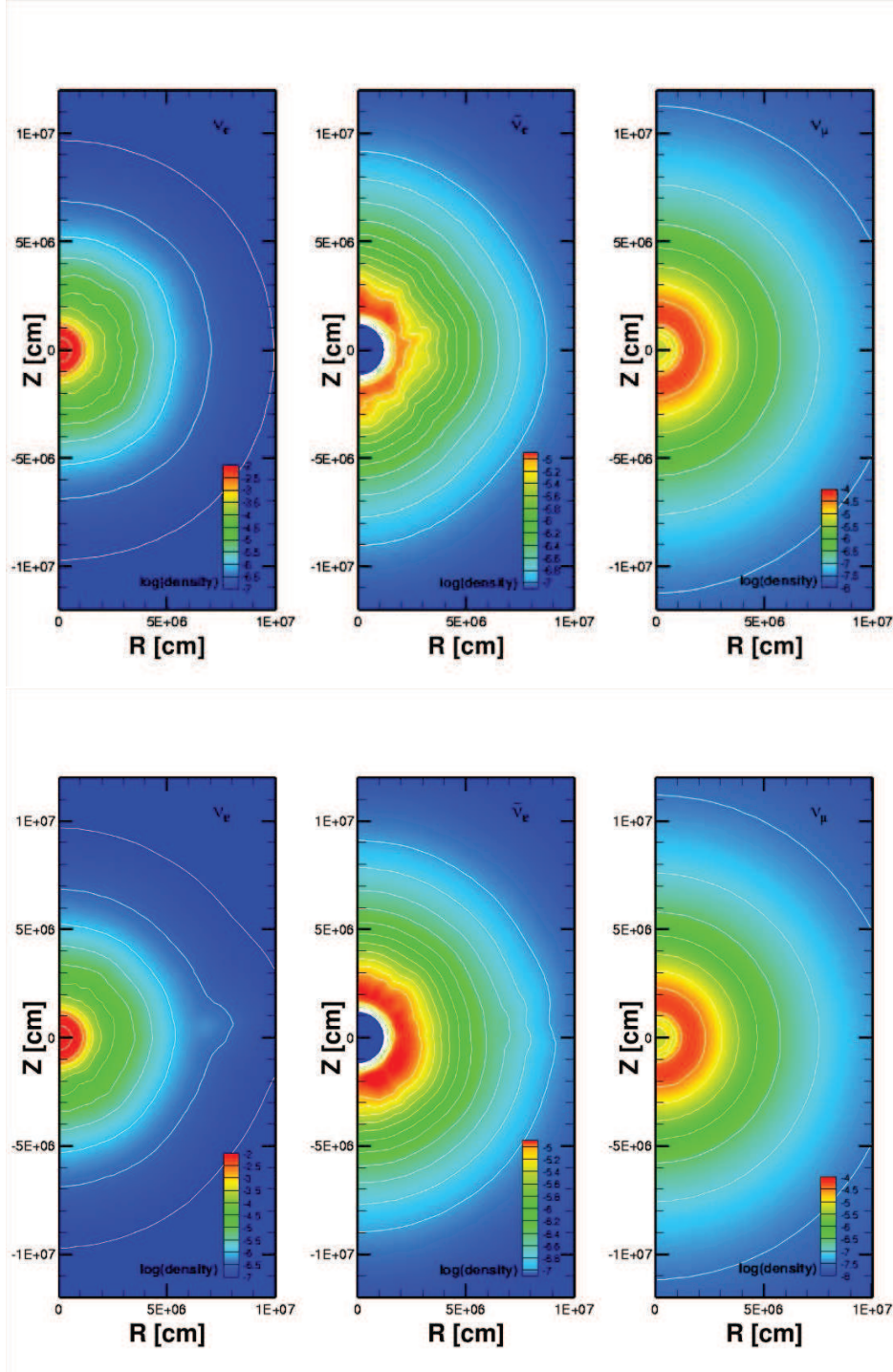


Fig. 8.— Profiles of neutrino density for the 3D supernova core at 150 ms after the bounce are shown on the slice of $\phi=51^\circ$ (top) and 141° (bottom). The neutrino density in log scale in the unit of fm^{-3} for three species (ν_e , $\bar{\nu}_e$ and ν_μ) is plotted by color maps in the left, middle and right panels, respectively.

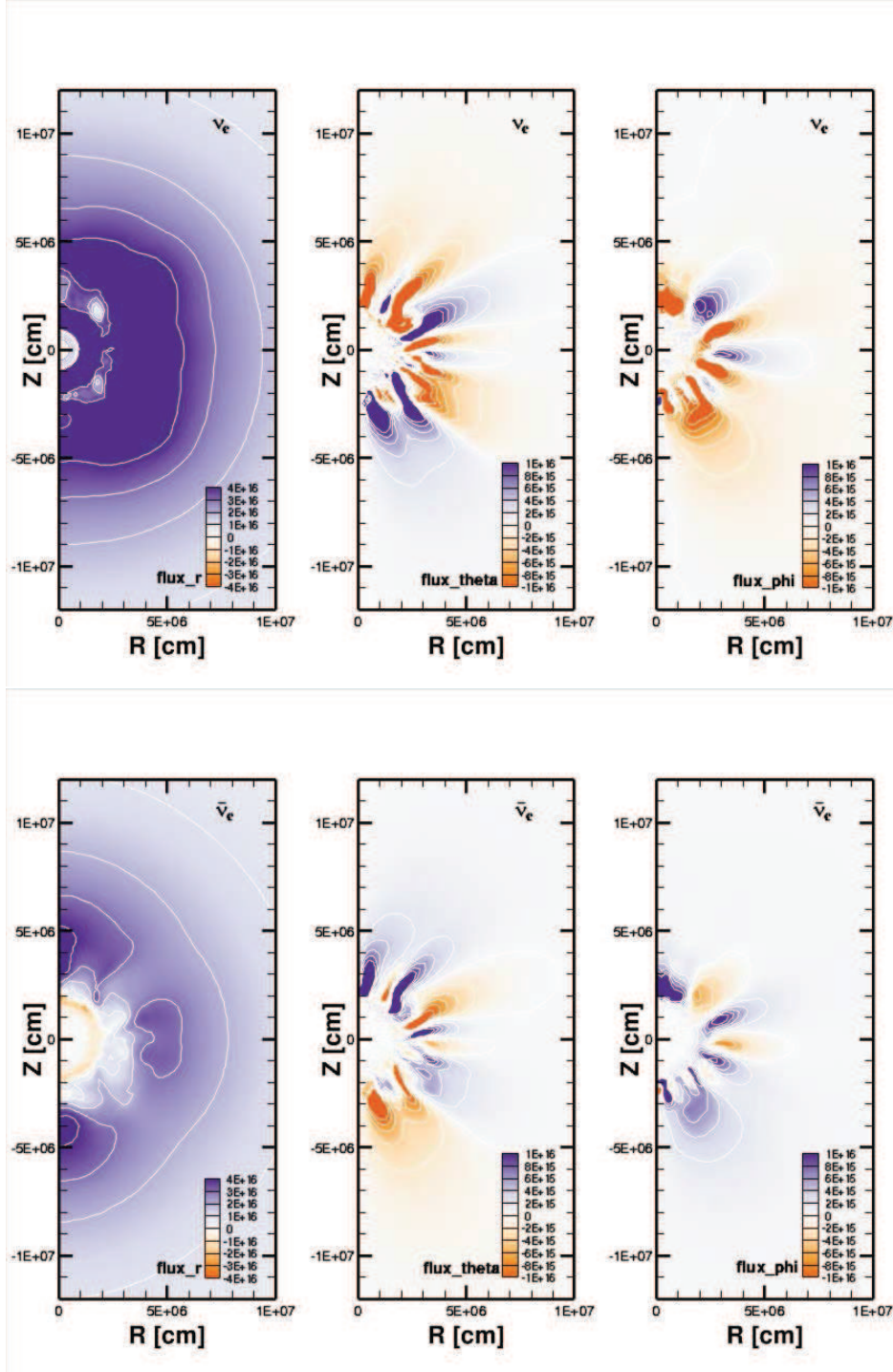


Fig. 9.— Profiles of number flux of ν_e (top) and $\bar{\nu}_e$ (bottom) in the unit of $\text{fm}^{-2}\text{s}^{-1}$ for the 3D supernova core at 150 ms after the bounce are shown on the slice of $\phi=51^\circ$. The radial, polar and azimuthal fluxes are plotted by color maps in the left, middle and right panels, respectively.

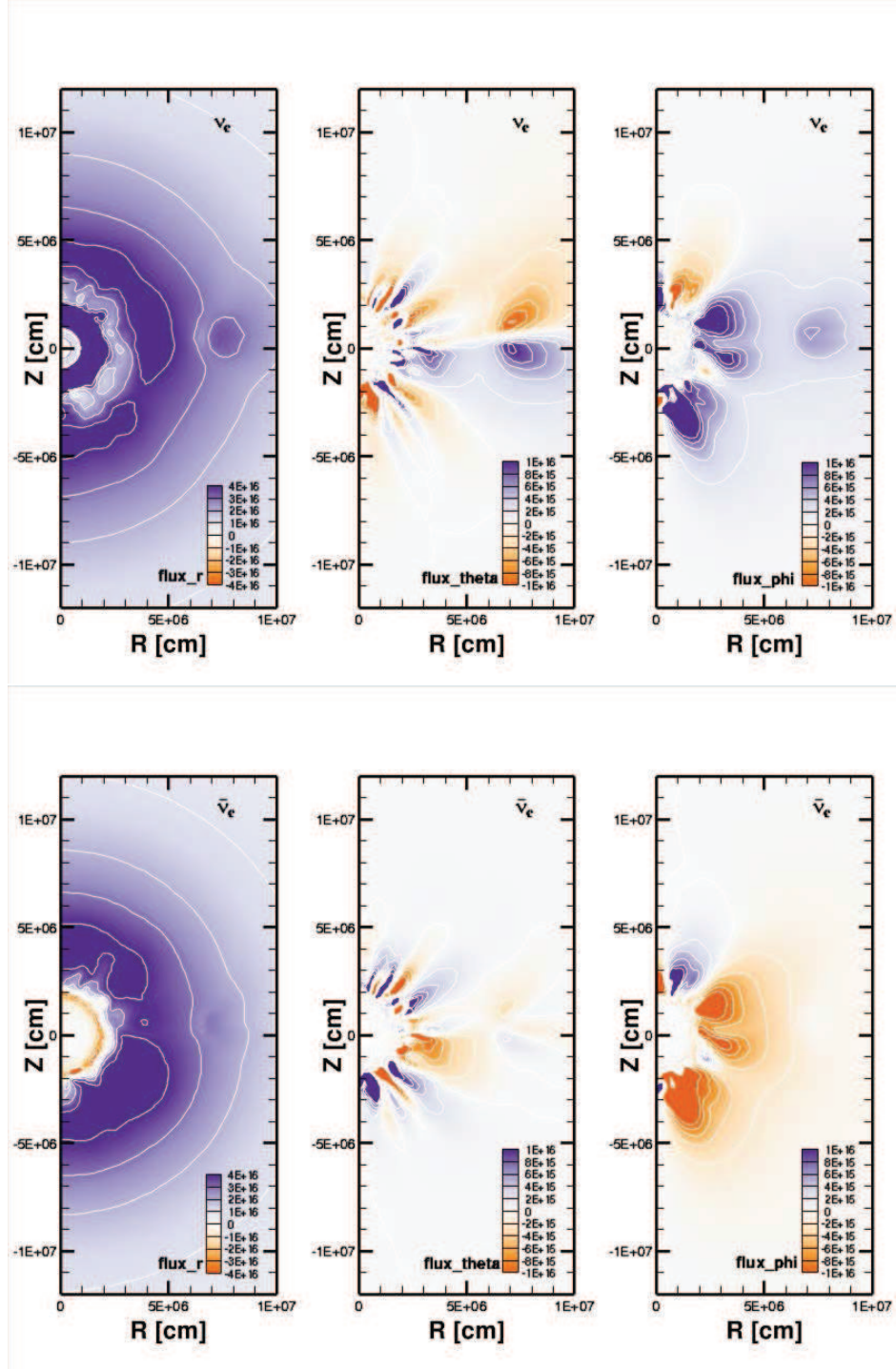


Fig. 10.— Same as Figure 9 but on the slice of $\phi=141^\circ$.

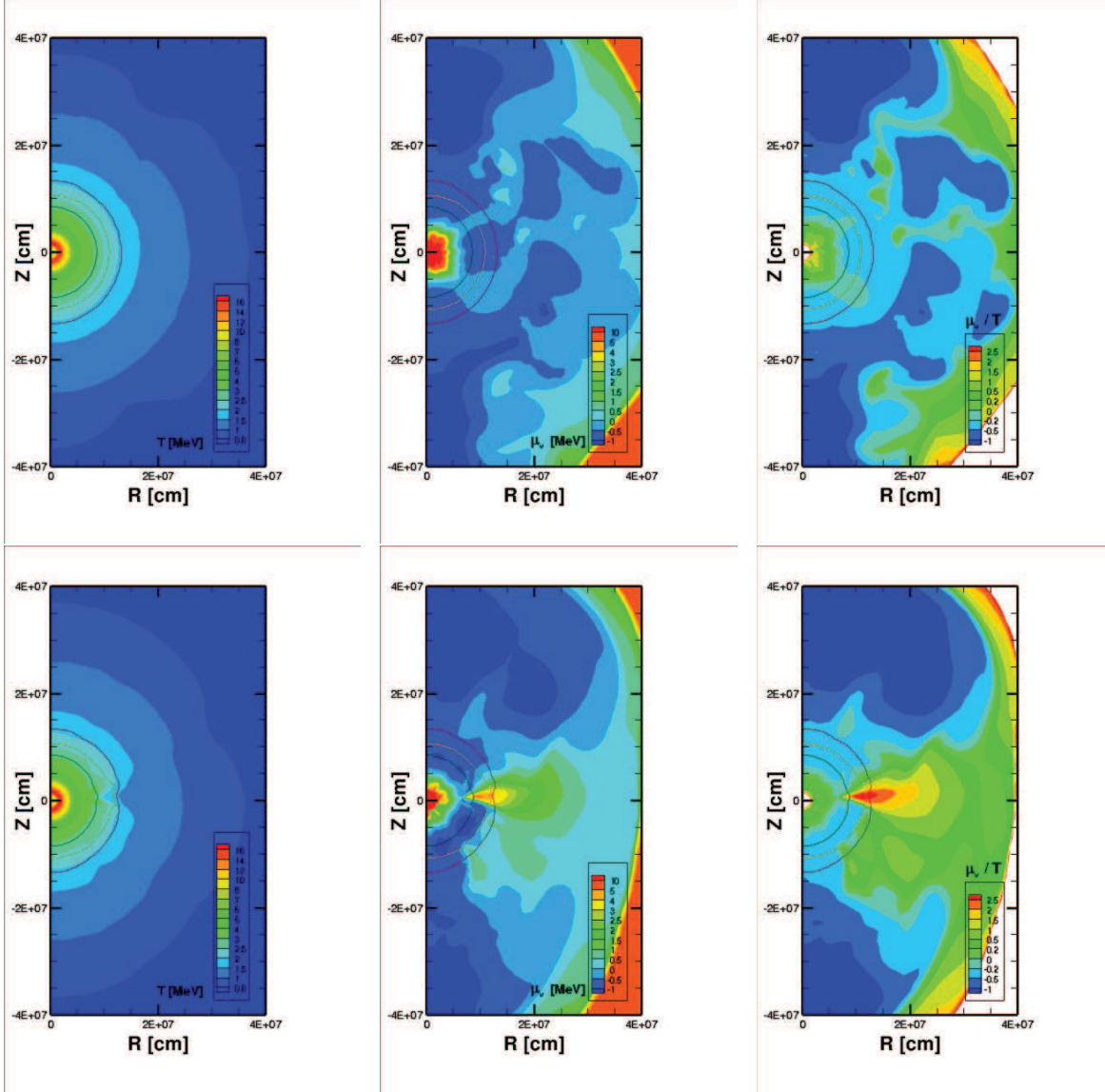


Fig. 11.— Profiles of temperature [MeV] (left), chemical potential [MeV] (center) and degeneracy of neutrinos (right) with the location of neutrino-sphere are shown for the 3D supernova core at 150 ms after the bounce on the slices of $\phi=51^\circ$ (top) and 141° (bottom). The neutrino-spheres for ν_e , $\bar{\nu}_e$ and ν_μ are shown in the order from outside to the center.

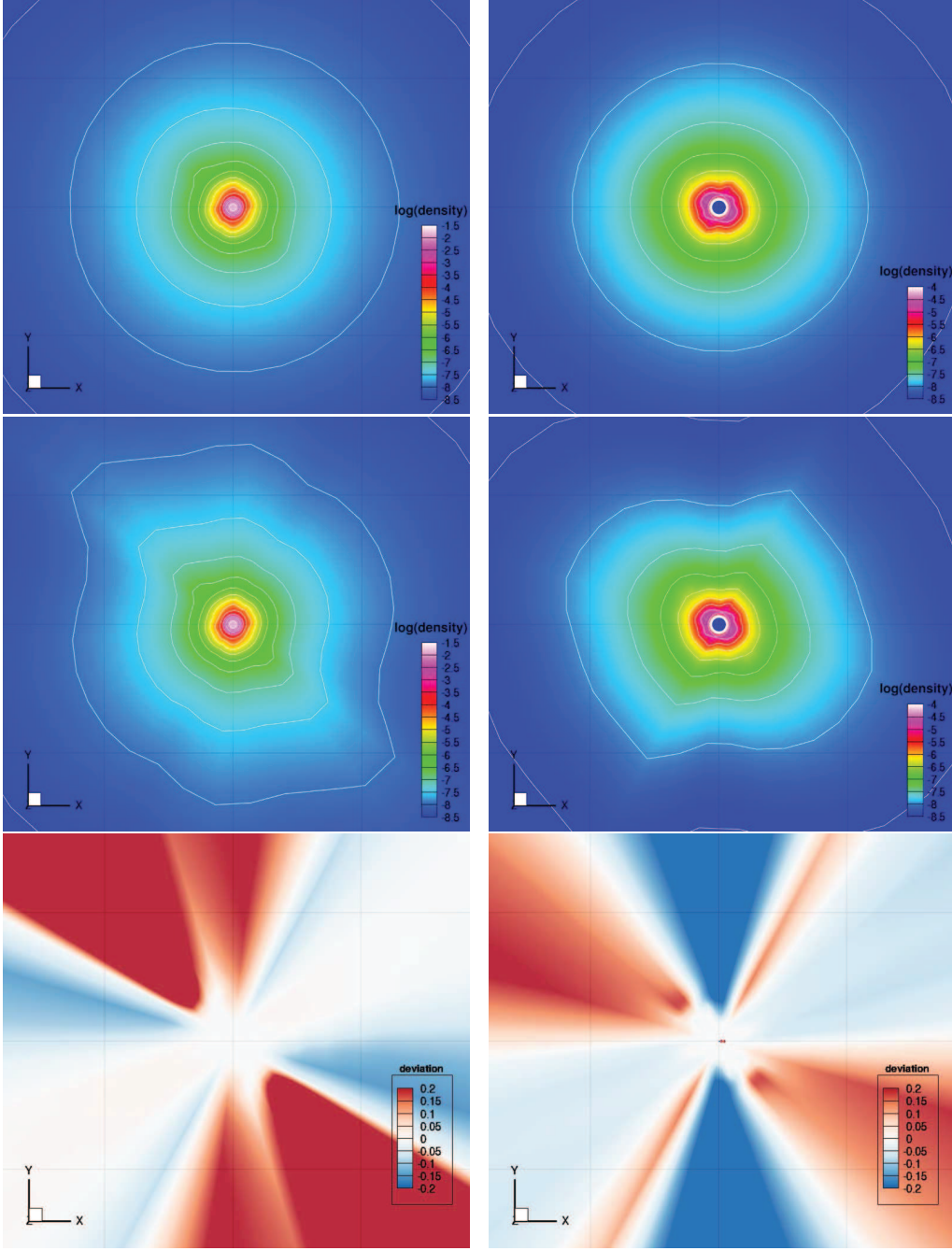


Fig. 12.— Comparison of the neutrino densities for two species (ν_e and $\bar{\nu}_e$) is displayed by color maps on the xy-plane ($z=0$) in the left and right panels, respectively. The setting of the 3D supernova core at 150 msec is the same as in Fig. 6. The neutrino densities evaluated by the 6D Boltzmann solver (top) and the ray-by-ray approximation (middle) are displayed together with the relative deviations between the two evaluations (bottom). Grid lines with 200 km spacing are shown in the background.

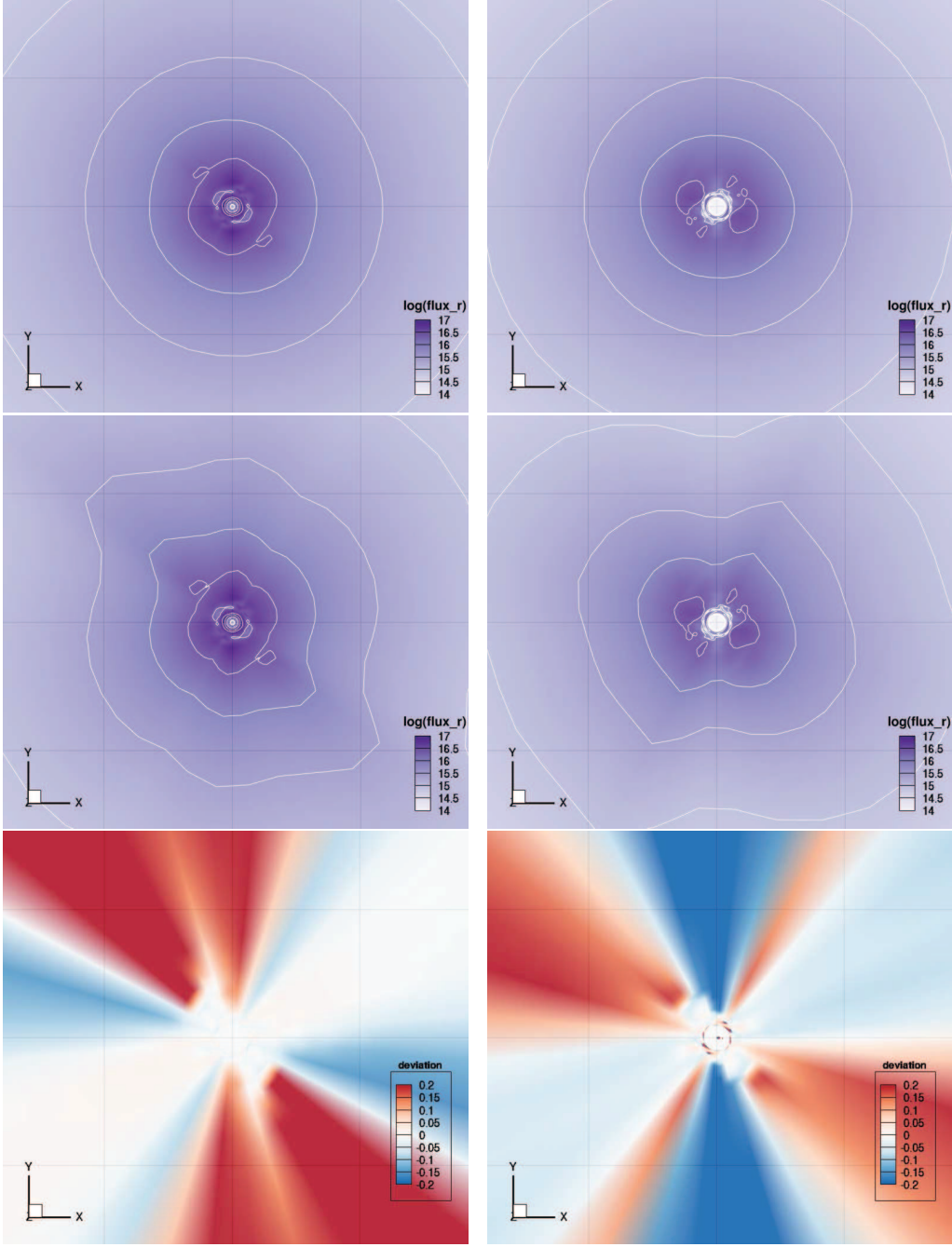


Fig. 13.— Comparison of the number fluxes in log scale in the unit of $\text{fm}^{-2}\text{s}^{-1}$ for two species (ν_e and $\bar{\nu}_e$) is displayed by color maps on the xy-plane ($z=0$) in the left and right panels, respectively. The setting of the 3D supernova core at 150 msec is the same as in Fig. 7. The number fluxes evaluated by the 6D Boltzmann solver (top) and the ray-by-ray approximation (middle) are displayed together with the relative deviations between the two evaluations (bottom). Grid lines with 200 km spacing are shown in the background.

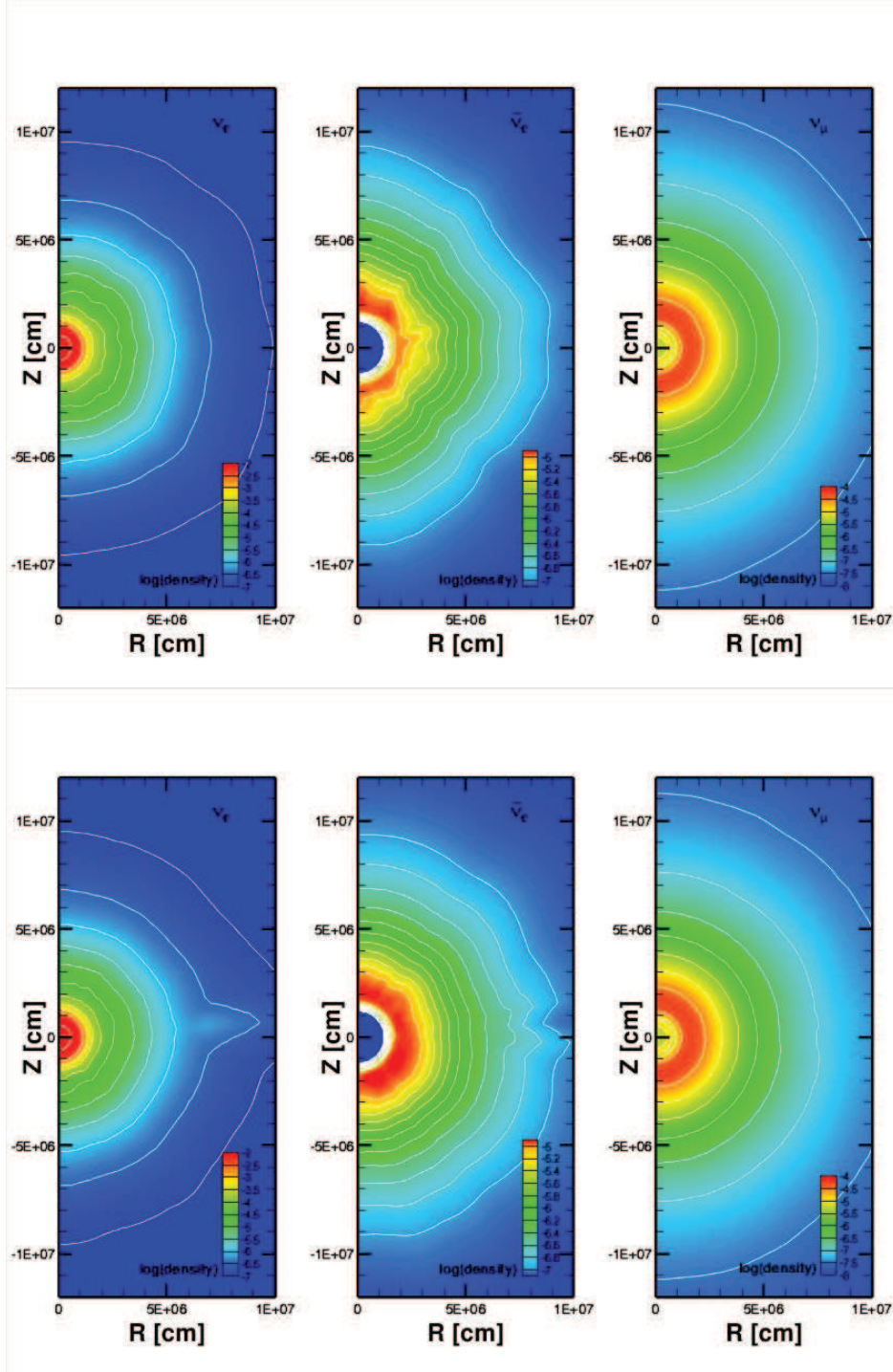


Fig. 14.— Profiles of the neutrino density evaluated by the ray-by-ray approximation with the same setting of the 3D supernova core at 150 msec used in Fig. 8. The locations of slice and the notation are the same as in Fig. 8.

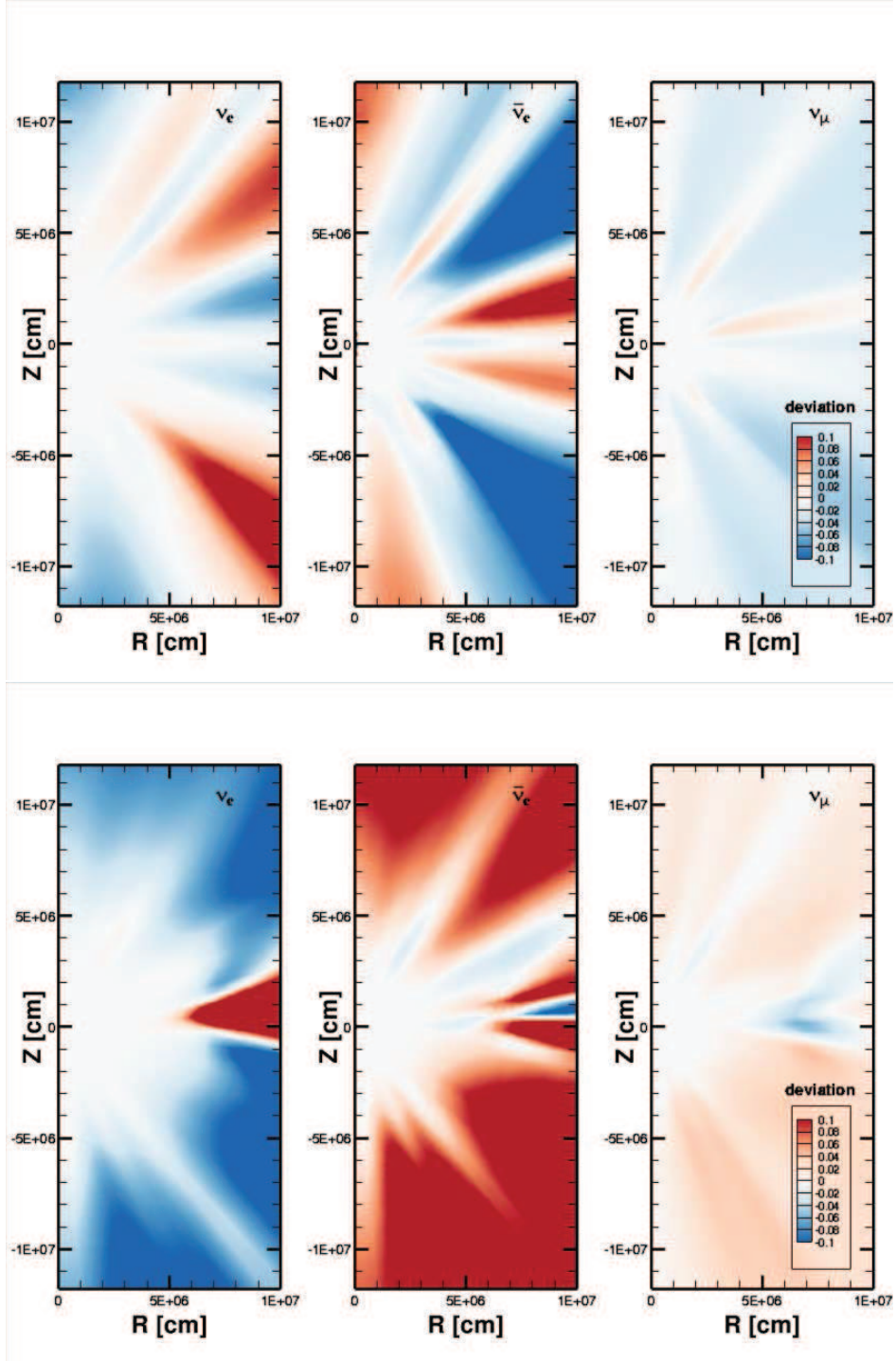


Fig. 15.— Color maps for the deviation of the neutrino density of the ray-by-ray approximation with respect to the 6D Boltzmann evaluation for the 3D supernova core at 150 msec corresponding to Figs. 8 and 14.

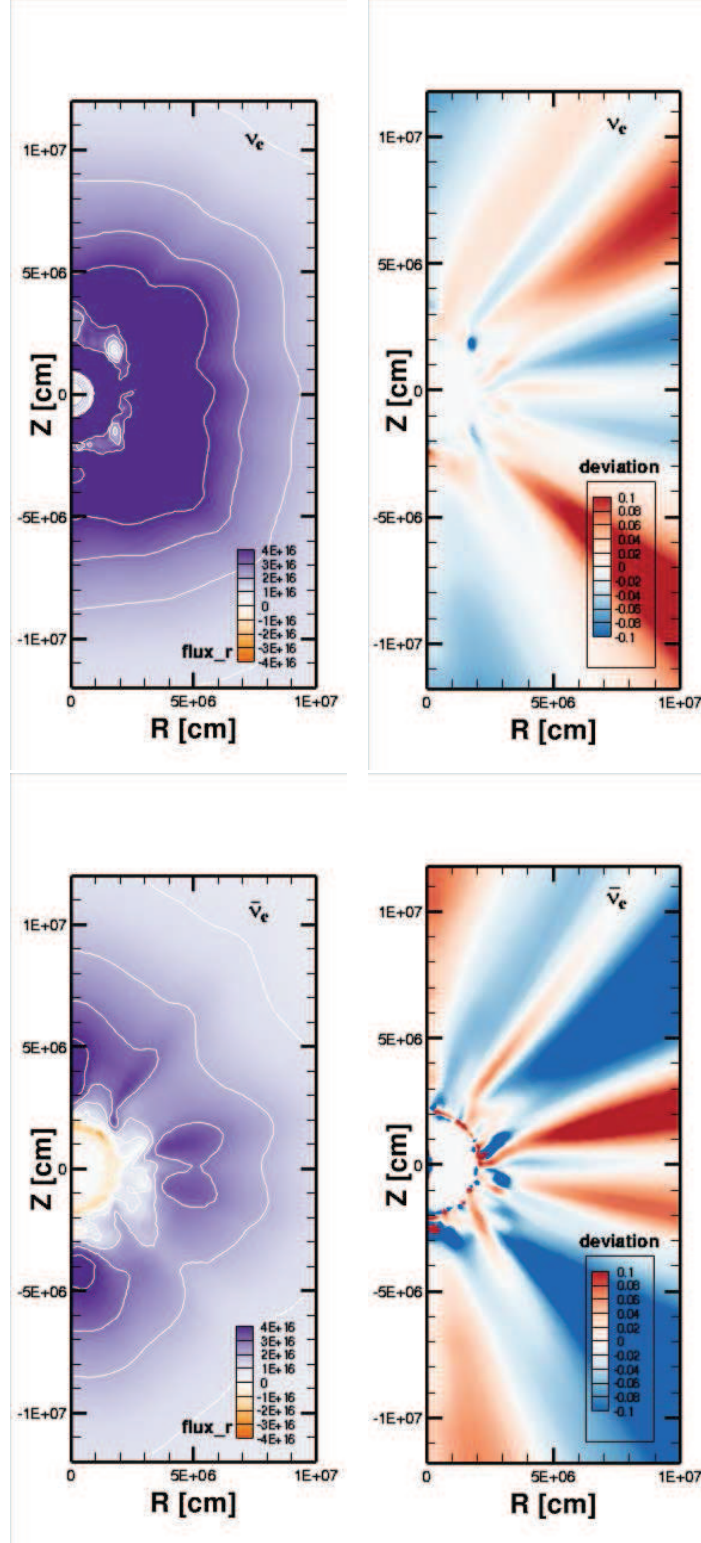


Fig. 16.— Profiles of the number flux of ν_e (top) and $\bar{\nu}_e$ (bottom) in the ray-by-ray approximation and its deviations with respect to the 6D Boltzmann evaluation are shown in left and right panels for the 3D supernova core at 150 msec on the slice of $\phi=51^\circ$ used in Fig. 9.

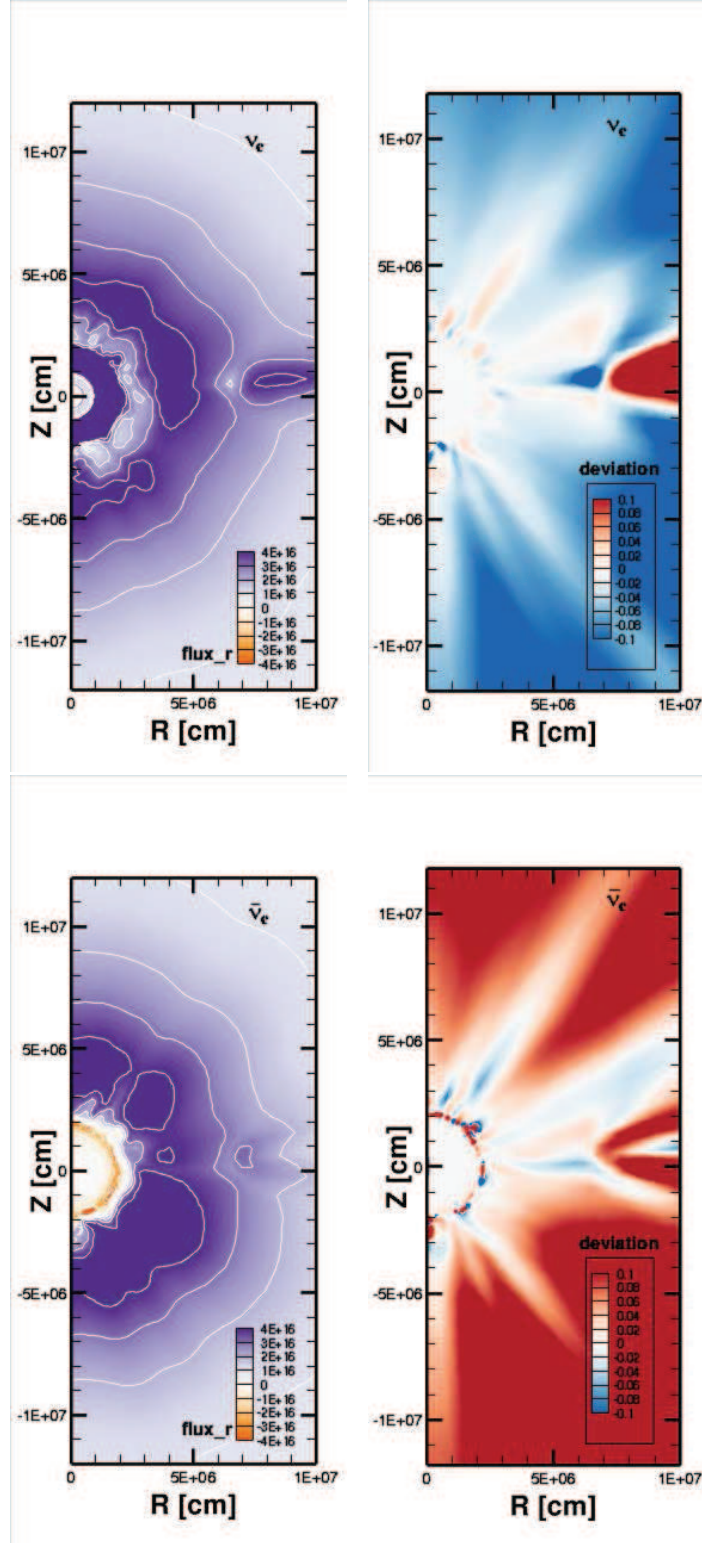


Fig. 17.— Same as Figure 16 but on the slice of $\phi=141^\circ$.

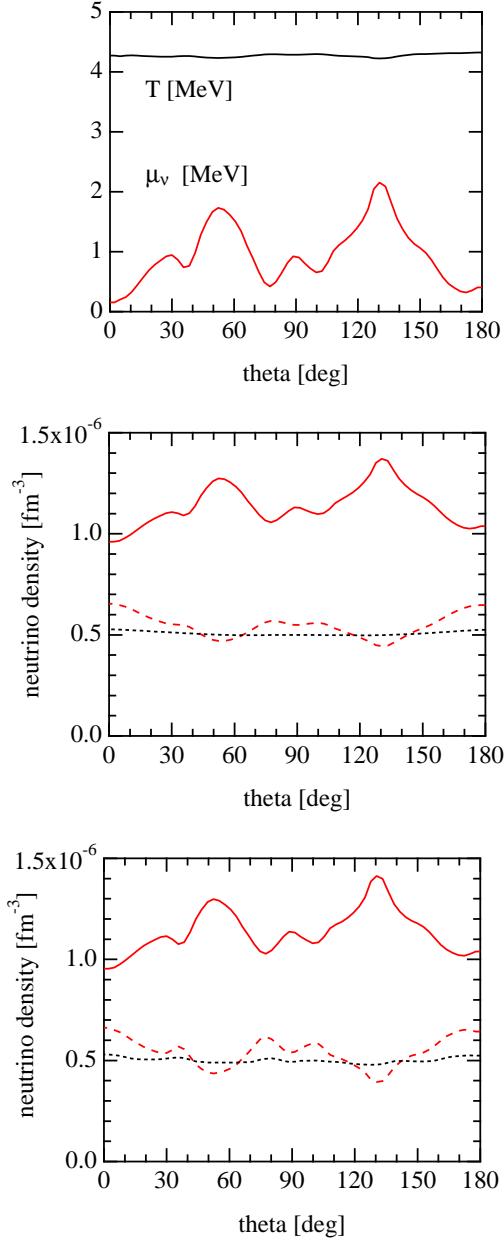


Fig. 18.— Distributions of temperature and neutrino chemical potential (top) and the neutrino densities by 6D Boltzmann (middle) and ray-by-ray evaluations (bottom) are plotted as functions of polar angle at the radius of 54 km on the slice of $\phi=51^\circ$. For the distributions in the middle and bottom panels, red solid, red dashed and block dotted lines denote densities for ν_e , $\bar{\nu}_e$ and ν_μ , respectively.

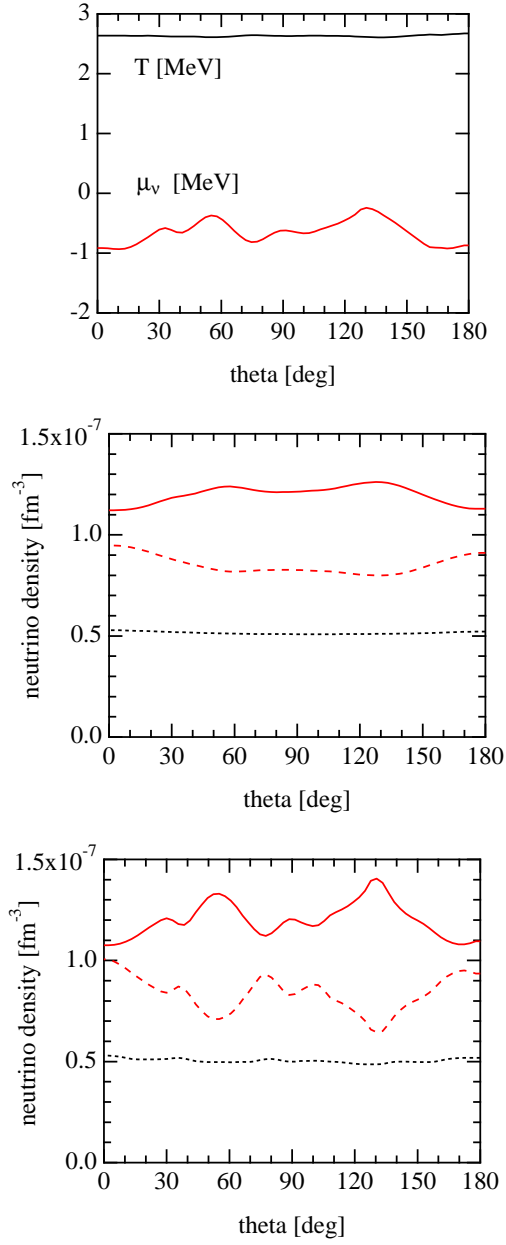


Fig. 19.— Same as Fig. 18, but at the radius of 94 km.

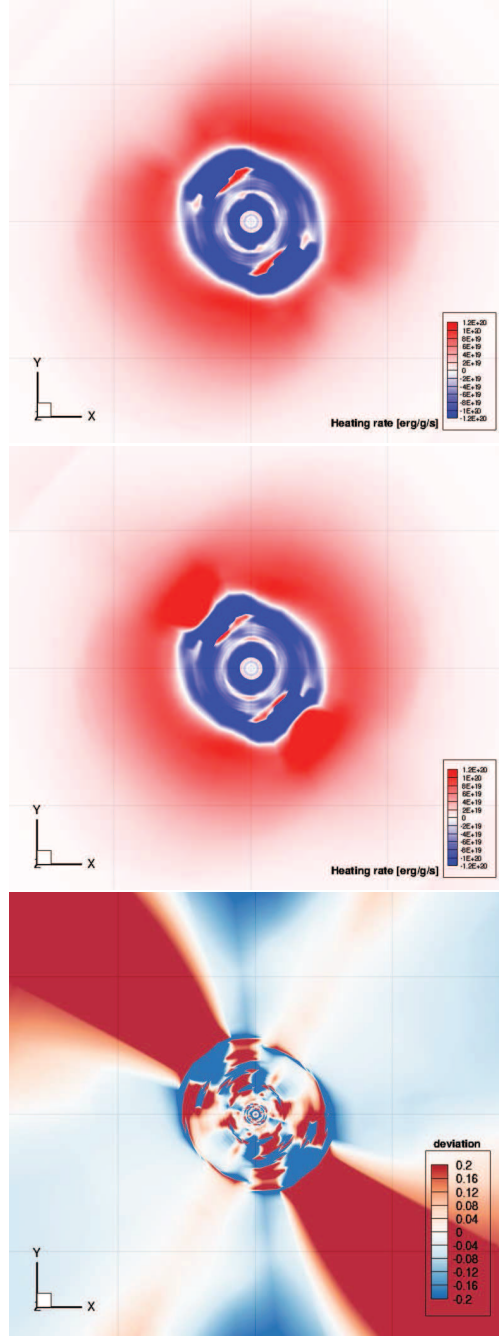


Fig. 20.— Contour maps for the neutrino heating on the xy-plane are shown for the 3D supernova core at 150 ms after the bounce. The top and middle panels display the energy transfer rates via neutrinos (heating and cooling by red and blue) evaluated by the 6D Boltzmann solver and the ray-by-ray approximation, respectively. The relative deviation of the ray-by-ray evaluation with respect to the 6D Boltzmann evaluation is shown in the bottom panel. Grid lines with 200 km spacing are shown in the background.

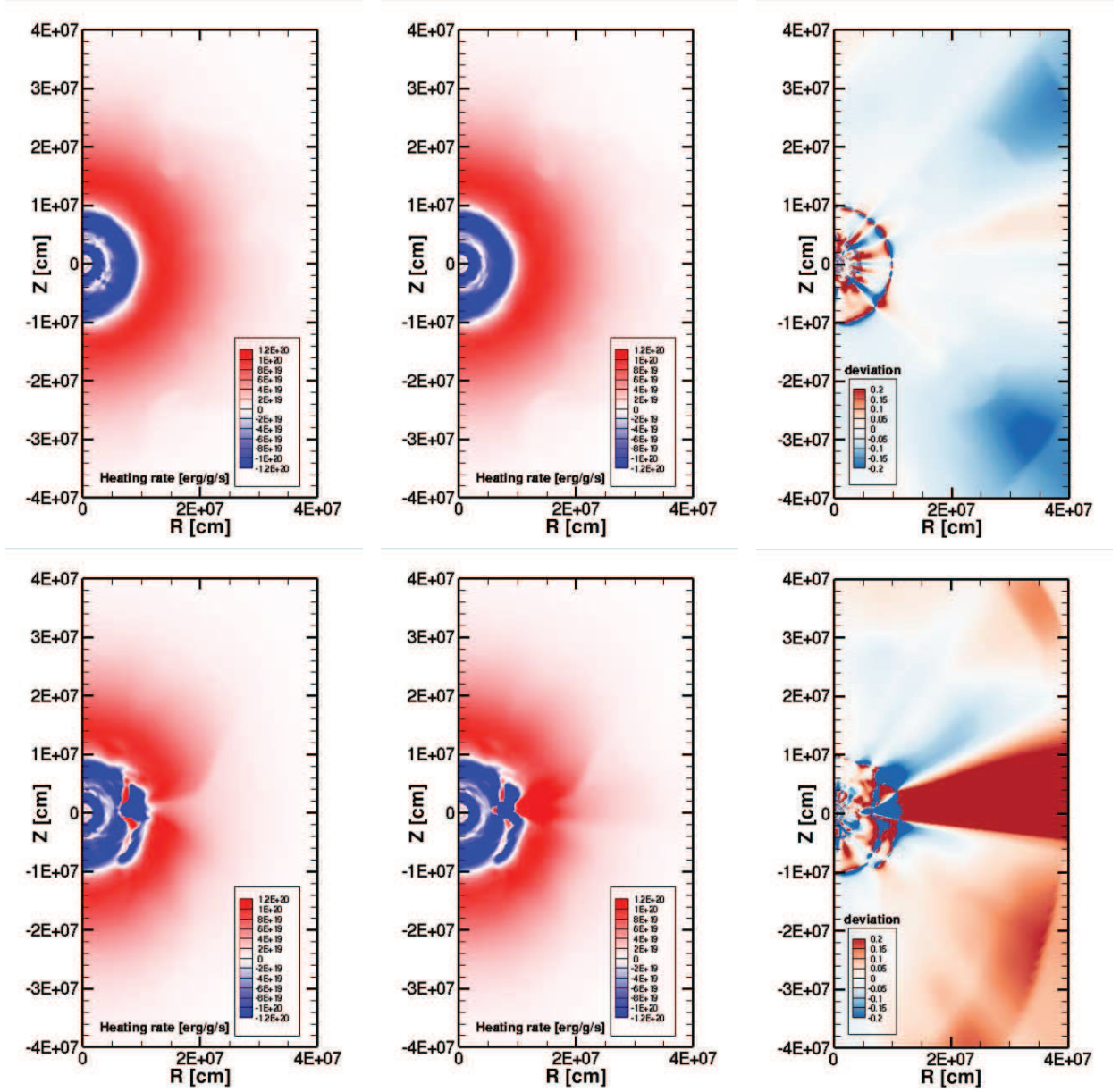


Fig. 21.— Contour maps for the neutrino heating on ϕ -slice at $\phi=51^\circ$ and 141° are shown for the 3D supernova core at 150 ms after the bounce in the upper and lower panels, respectively. The left and middle panels display the energy transfer rates via neutrinos evaluated by the 6D Boltzmann solver and the ray-by-ray approximation, respectively. The relative deviation of the ray-by-ray evaluation with respect to the 6D Boltzmann evaluation is shown in the right panel.

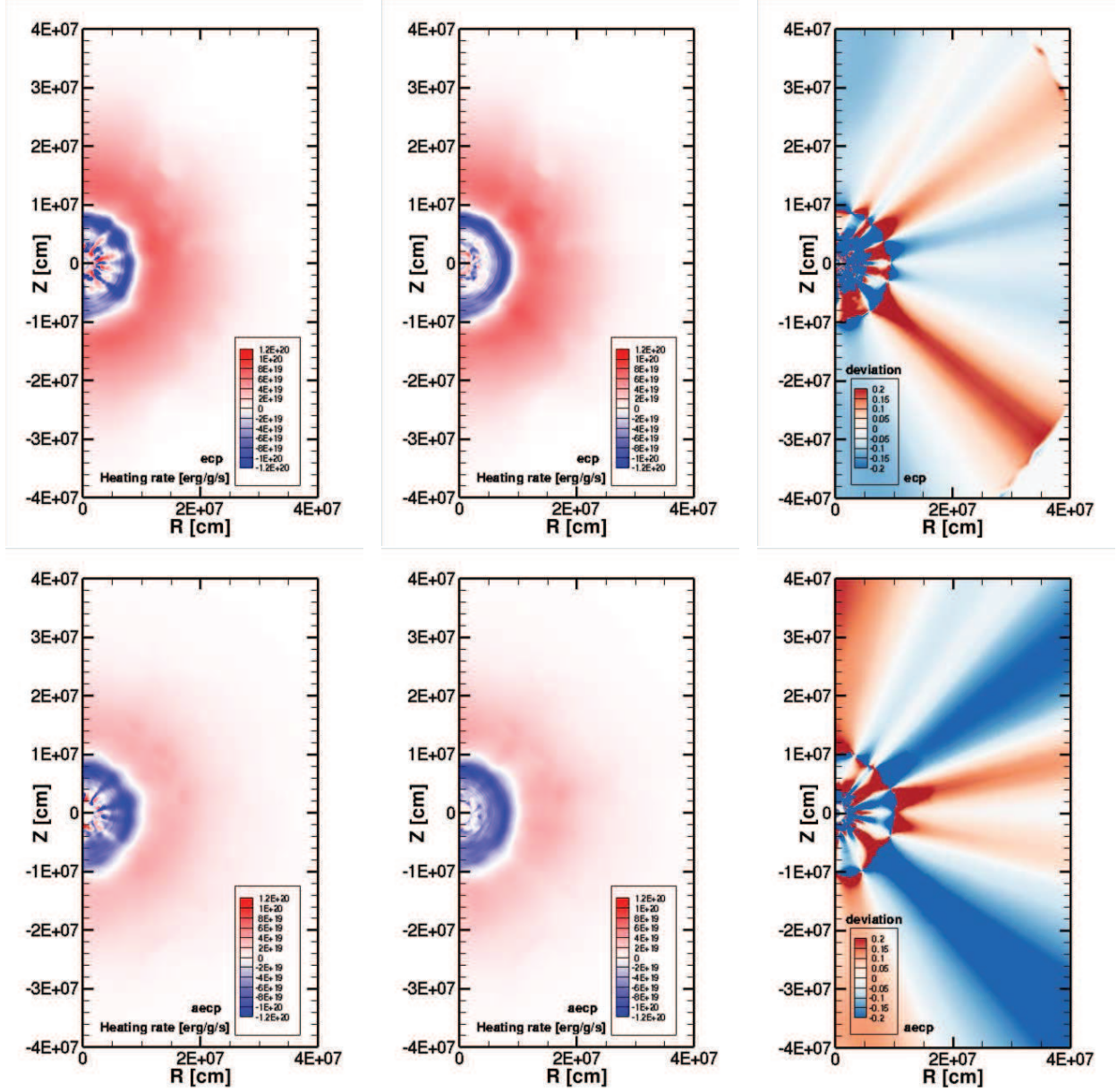


Fig. 22.— Contour maps for the heating rate via ν_e and $\bar{\nu}_e$ absorptions on ϕ -slice at $\phi=51^\circ$ are shown in the upper and lower panels, respectively. The left and middle panels display the 6D Boltzmann and ray-by-ray evaluations together with the relative deviation of the ray-by-ray evaluation in the right panel.

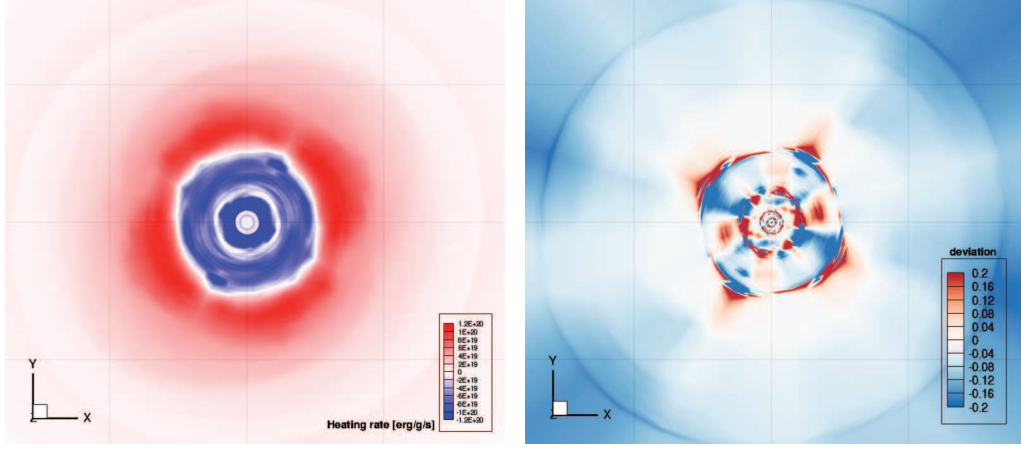


Fig. 23.— Contour maps of the heating rate obtained by the 6D Boltzmann solver for the 3D supernova core at 100 ms after the bounce are shown in left panel. The relative deviation of the ray-by-ray evaluation is shown in right panel. Grid lines with 200 km spacing are shown in the background.

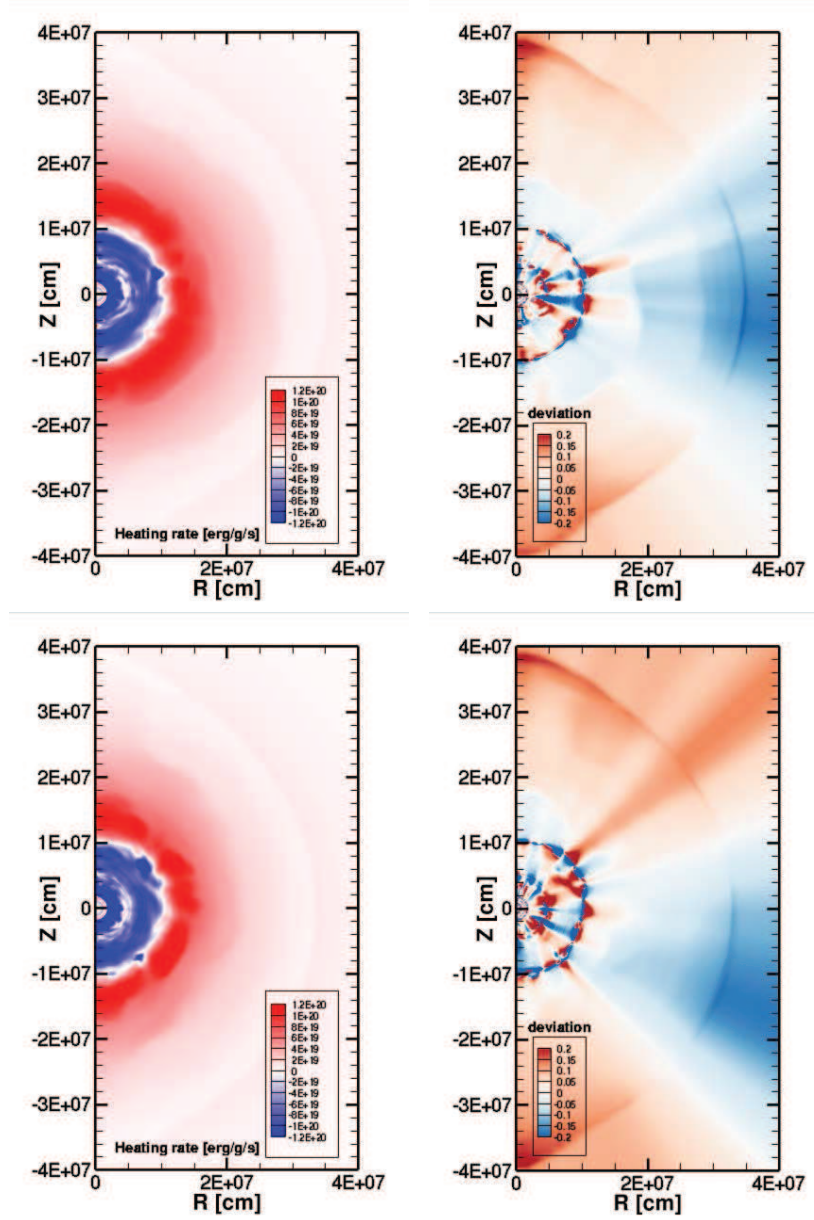


Fig. 24.— Color maps of the heating rate by the 6D Boltzmann evaluation are shown in the left panels for the 3D supernova core at 100 ms after the bounce. The corresponding profiles for the relative deviation of the ray-by-ray evaluation are shown in the right panels. The top and bottom panels show the profiles on ϕ -slice at $\phi = 51^\circ$ and 141° , respectively.

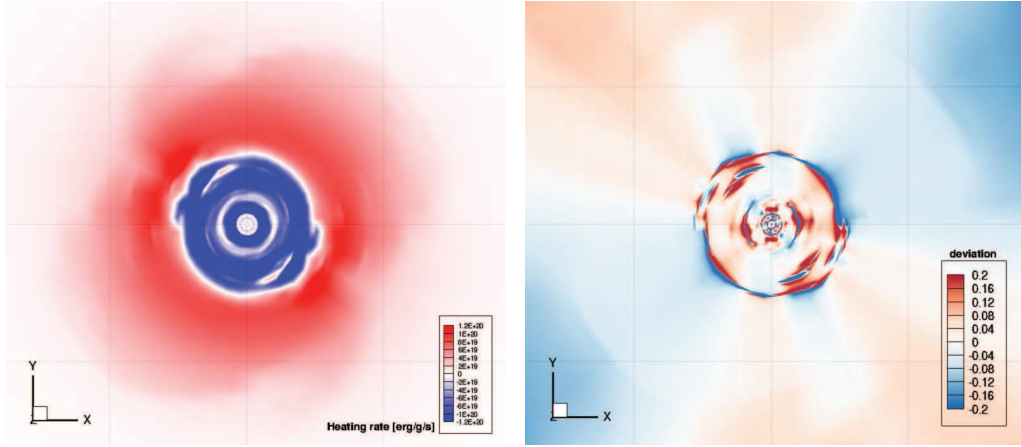


Fig. 25.— Same as Fig. 23 but for the 3D supernova core at 200 ms after the bounce.

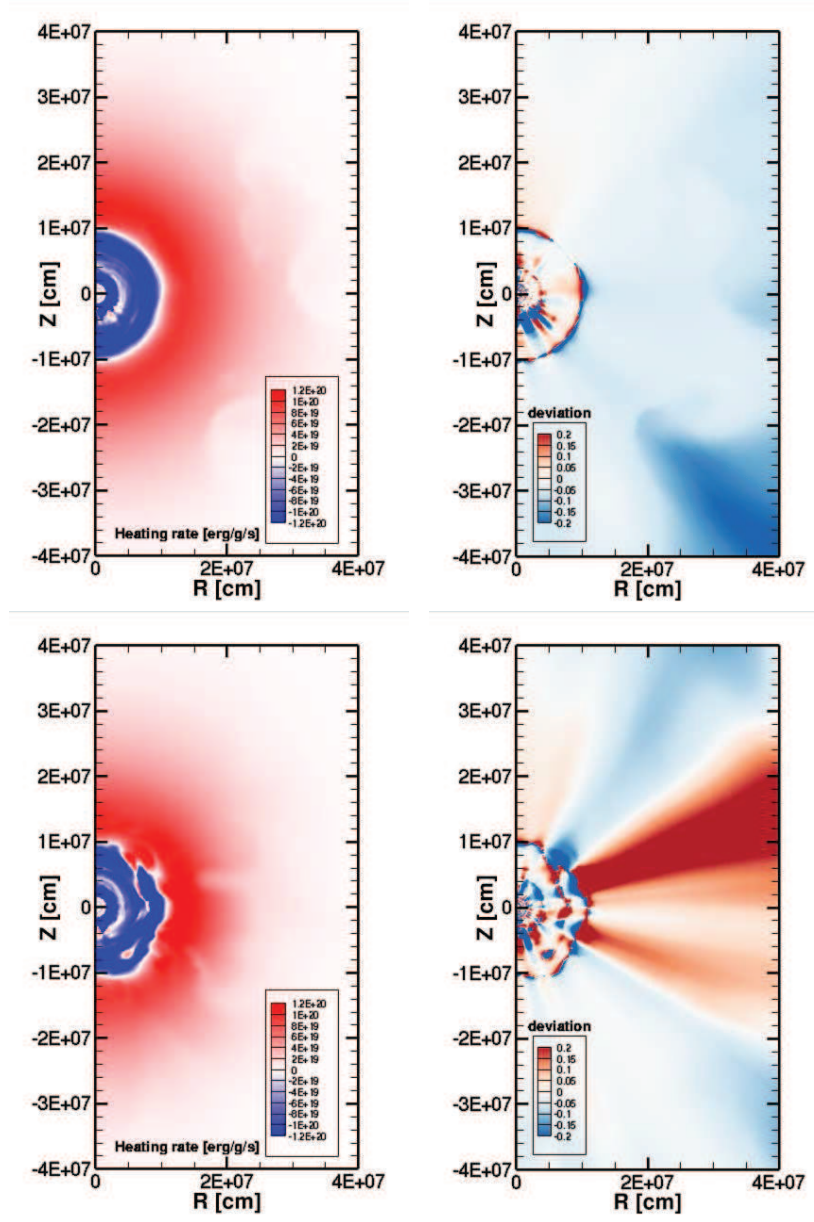


Fig. 26.— Same as Fig. 24 but for the 3D supernova core at 200 ms after the bounce.

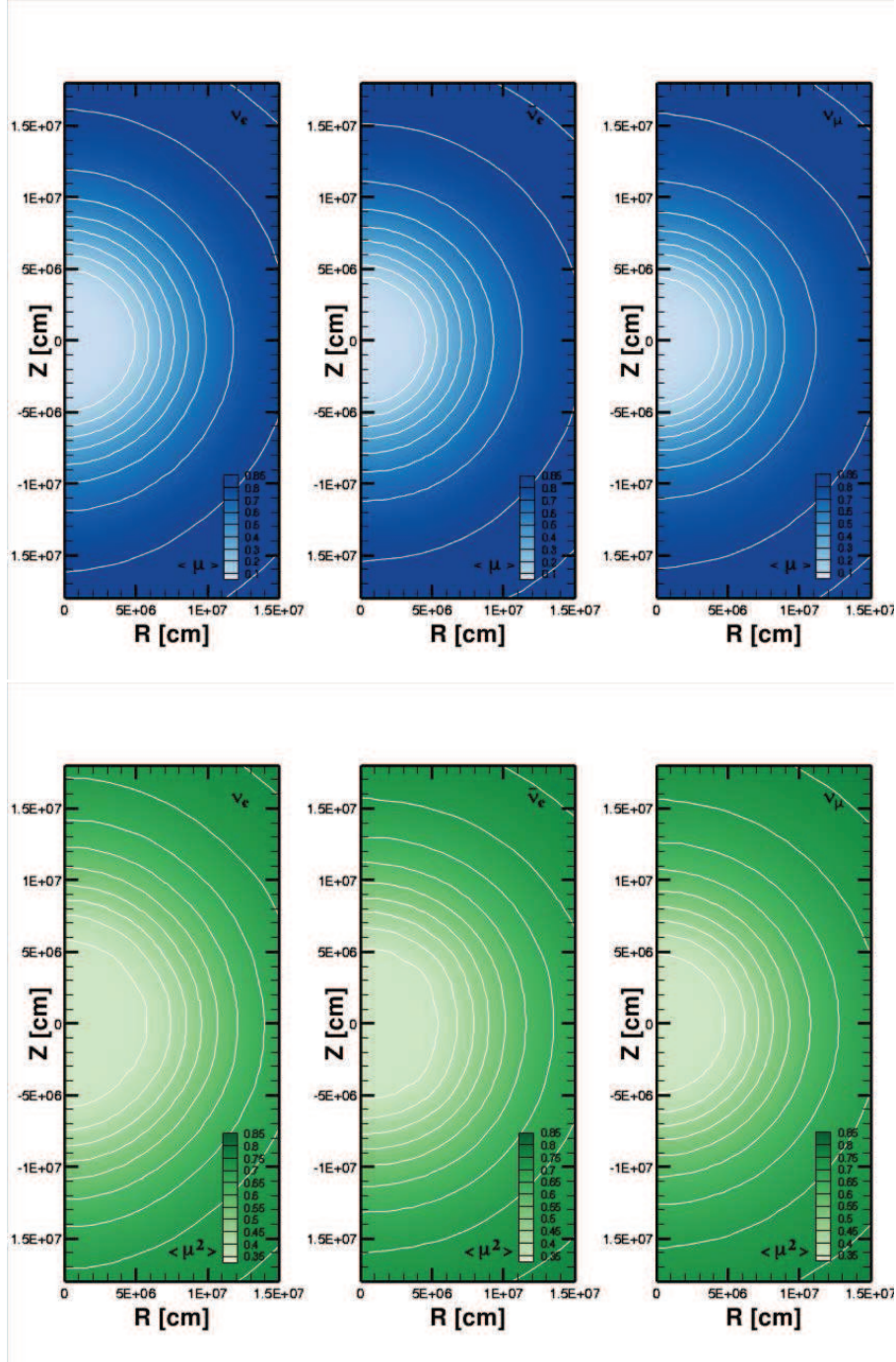


Fig. 27.— Contour maps of the flux factor, $\langle \mu \rangle$, (top) and the second moment of angle, $\langle \mu^2 \rangle$, (bottom) are shown for the 3D supernova core at 150 ms after the bounce on the slice of $\phi=51^\circ$. Left, middle and right panels display profiles for three species (ν_e , $\bar{\nu}_e$ and ν_μ), respectively.

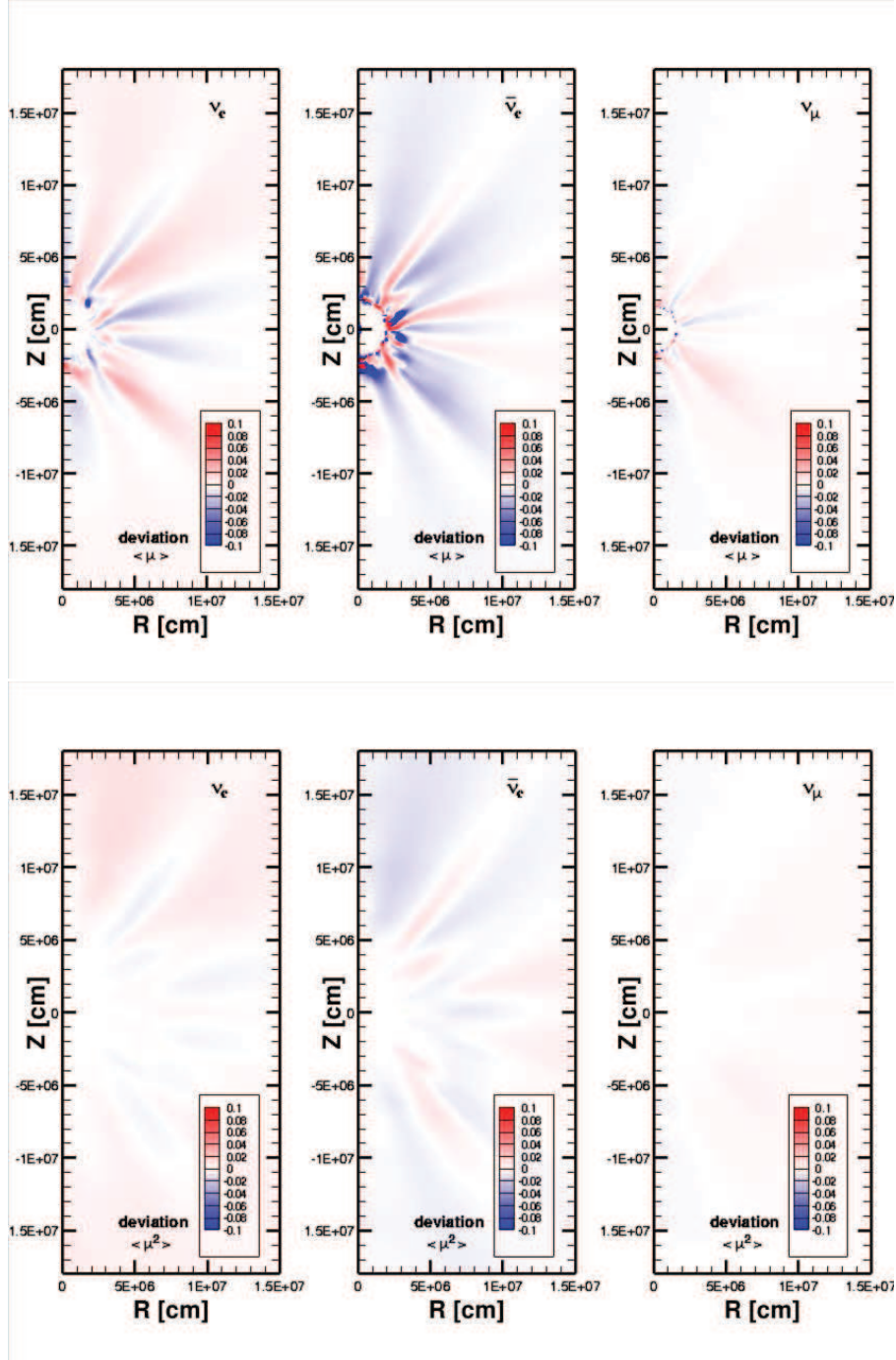


Fig. 28.— Contour maps of the relative deviations of the ray-by-ray evaluation with respect to the 6D Boltzmann evaluation are shown for the angle moments $\langle \mu_\nu \rangle$ (top) and $\langle \mu_\nu^2 \rangle$ (bottom). Left, middle and right panels display profiles for three species (ν_e , $\bar{\nu}_e$ and ν_μ), respectively, corresponding to those in Fig. 27.

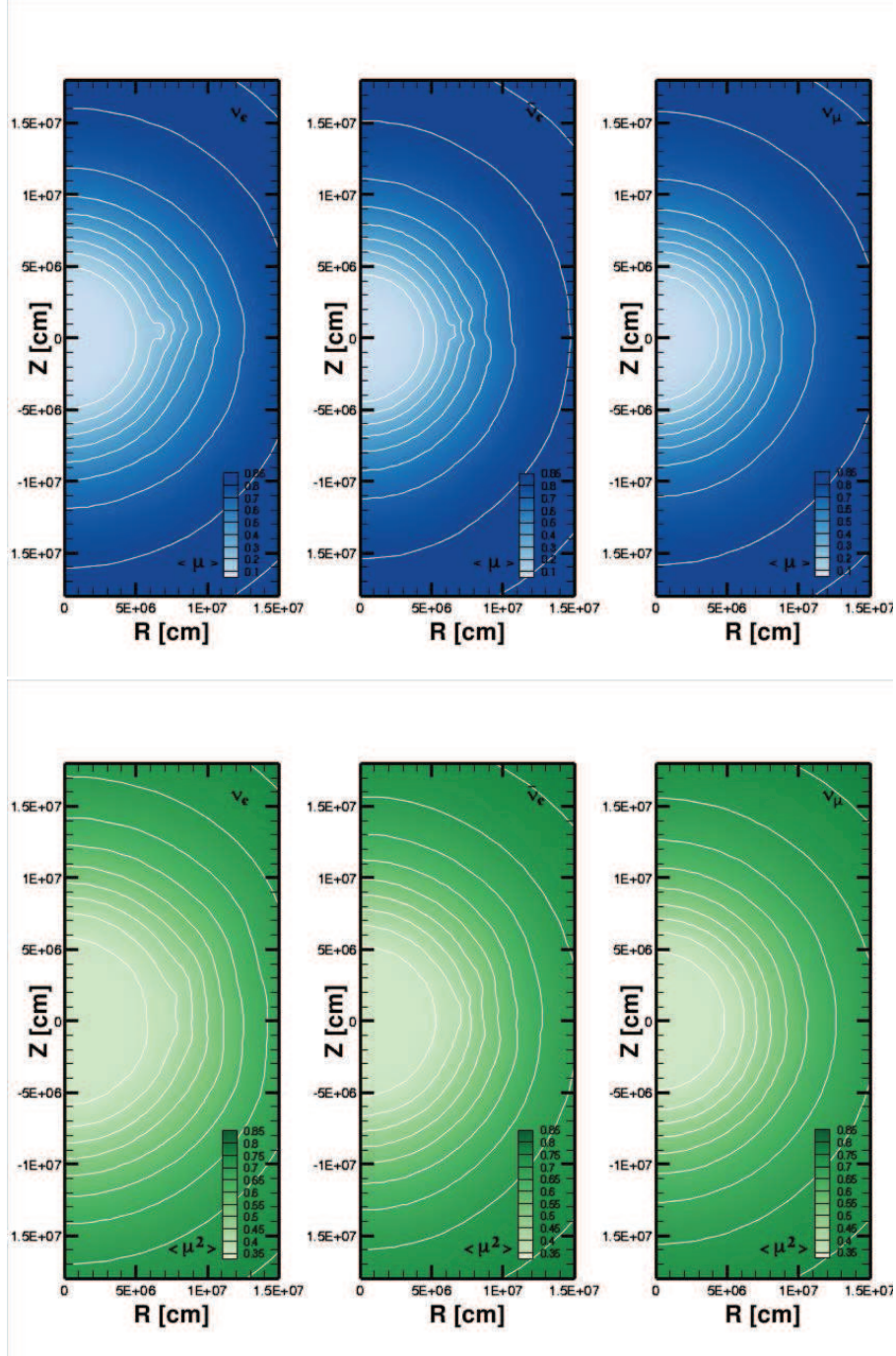


Fig. 29.— Same as Figure 27 but on the slice of $\phi=141^\circ$.

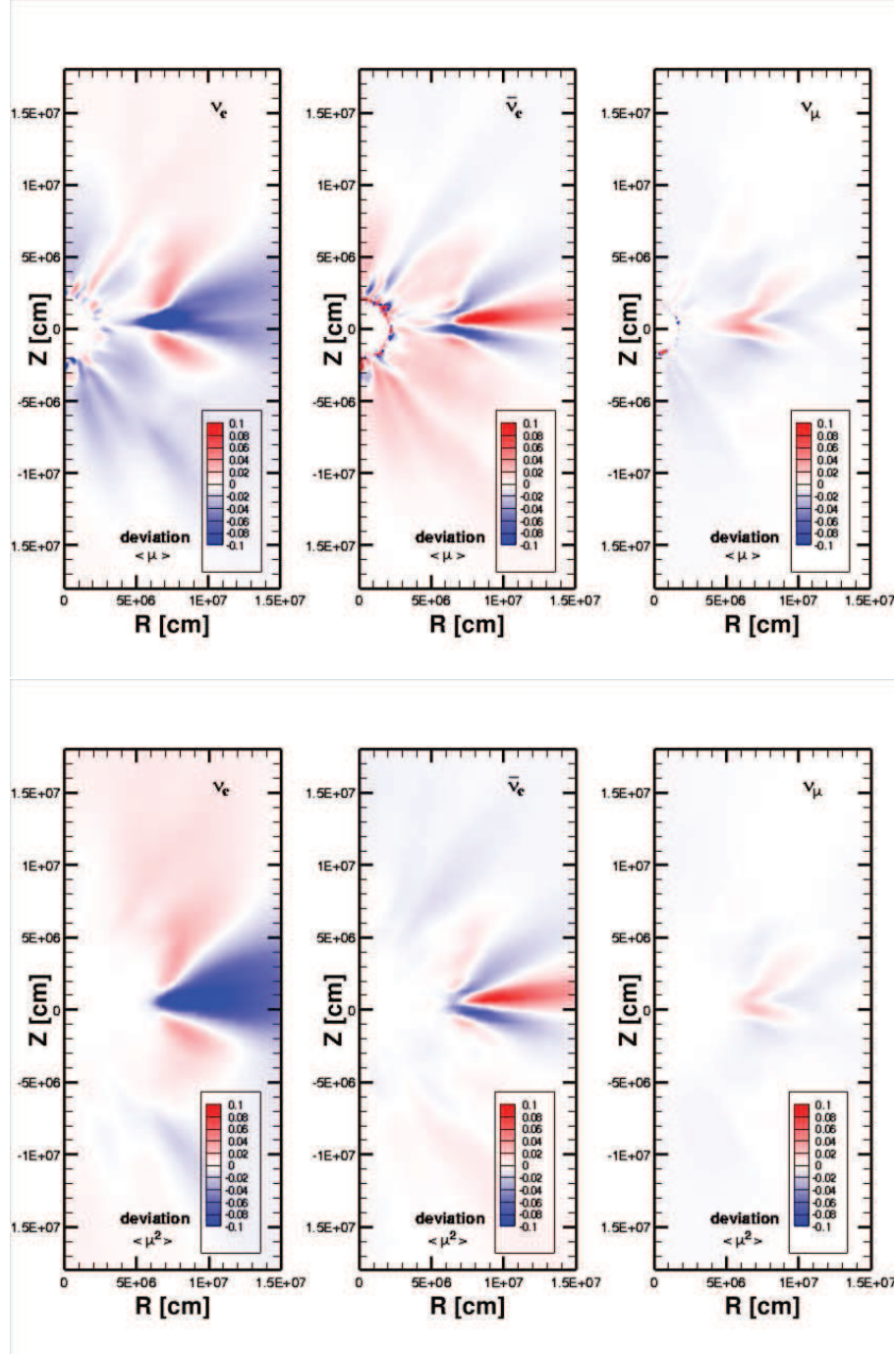


Fig. 30.— Same as Figure 28 but on the slice of $\phi=141^\circ$.

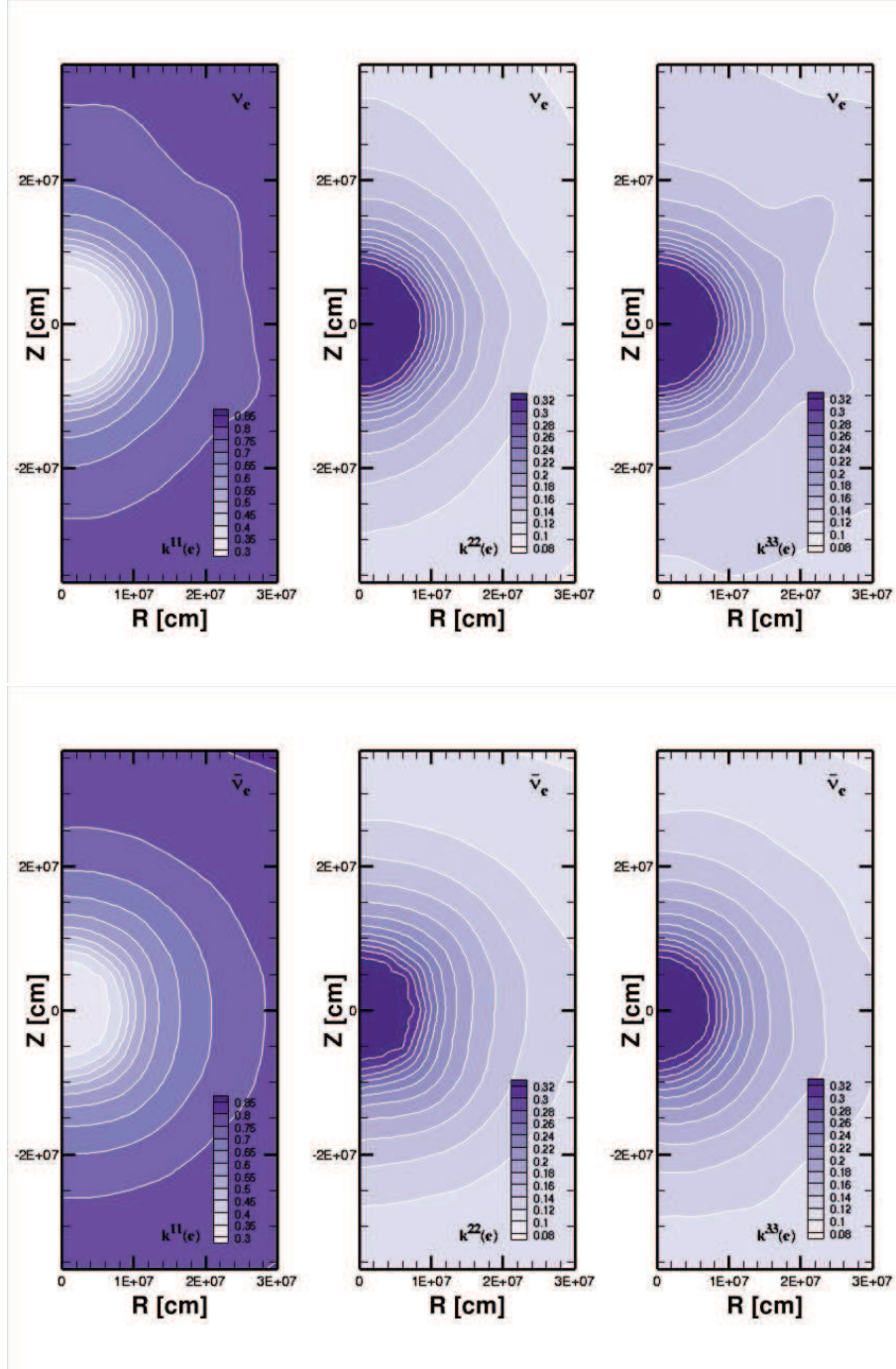


Fig. 31.— Contour maps of the Eddington tensor for the 3D supernova core at 150 ms after the bounce on the slice of $\phi=51^\circ$. The diagonal elements for the energy bin ($E_\nu = 34$ MeV) are shown in left (rr), middle ($\theta\theta$) and right ($\phi\phi$) panels. The profiles for two species ν_e and $\bar{\nu}_e$ are displayed in the top and bottom panels, respectively.

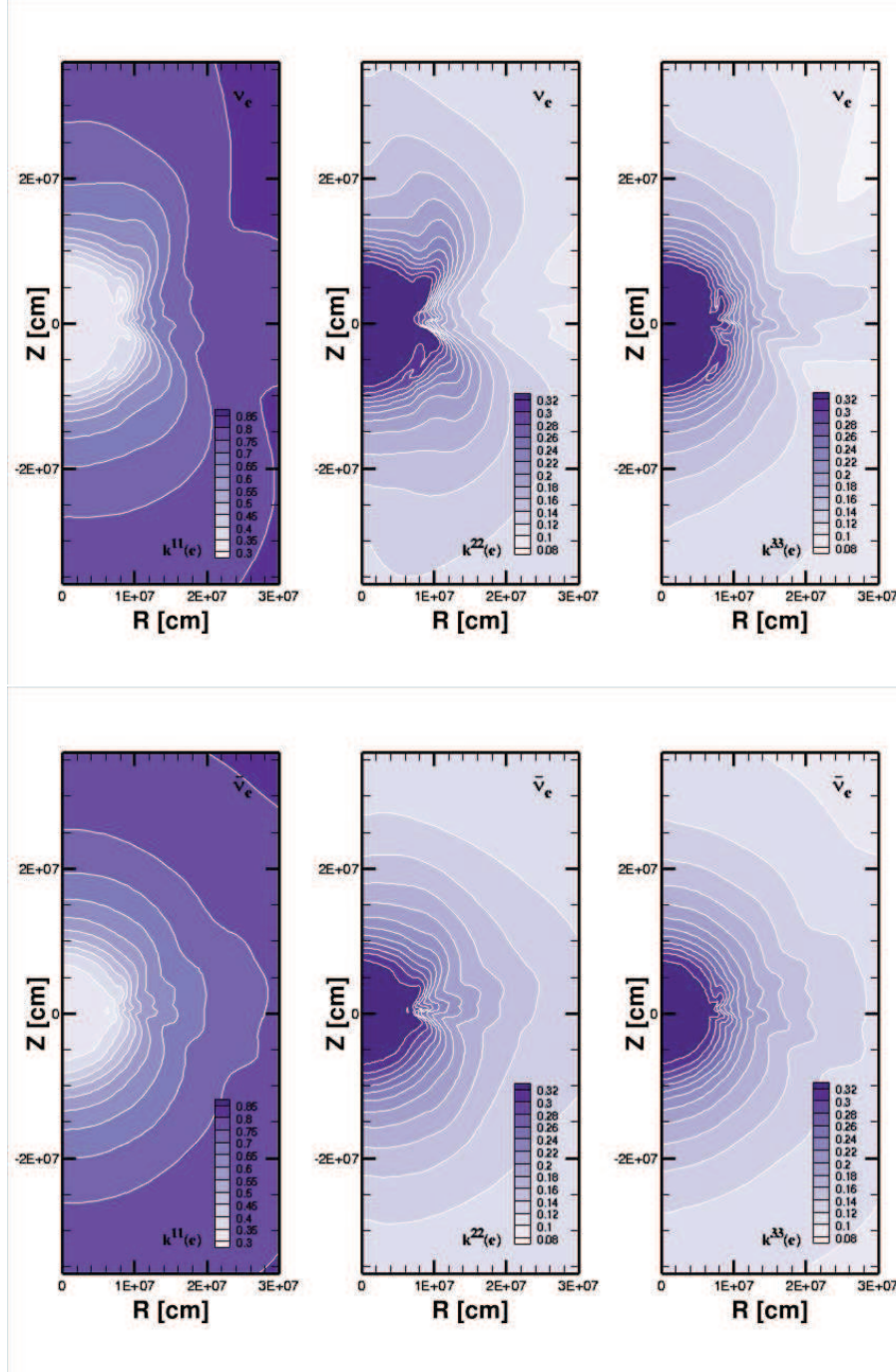


Fig. 32.— Same as Figure 31 but on the slice of $\phi = 141^\circ$.

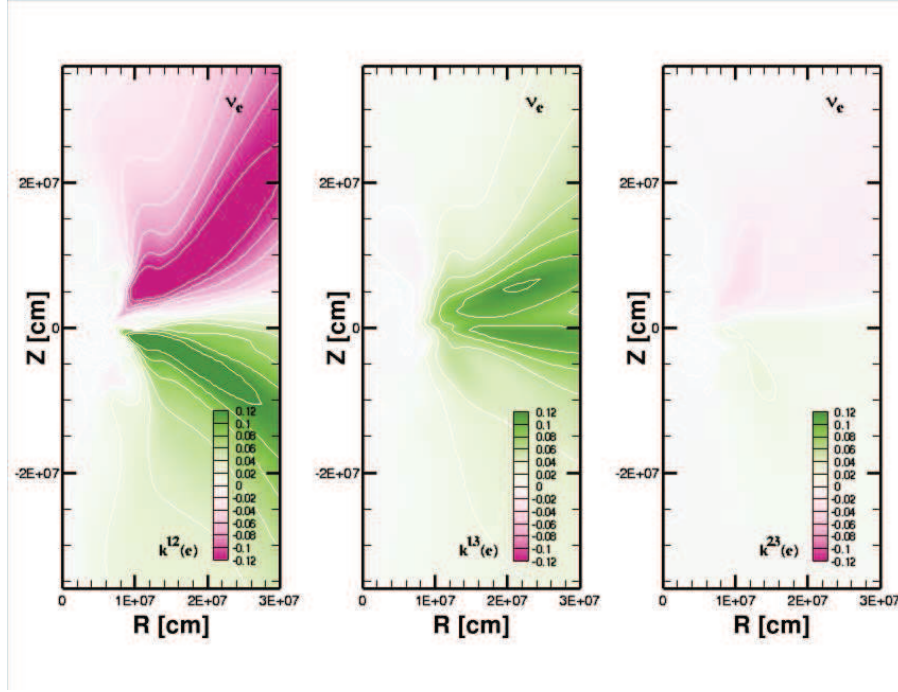


Fig. 33.— Contour maps of the Eddington tensor for the 3D supernova core at 150 ms after the bounce on the slice of $\phi=141^\circ$. The non-diagonal elements for the energy bin ($E_\nu = 34$ MeV) for ν_e are shown in left ($r\theta$), middle ($r\phi$) and right ($\theta\phi$) panels.